



Tracking crustal thickness at the sediment inundated edge of the Gawler Craton, South Australia

Shubham Agrawal^{a,*}, Caroline M. Eakin^a, John P. O'Donnell^{b,1}

^a Research School of Earth Sciences, Australian National University, 142 Mills Road, Canberra 2601, ACT, Australia

^b Geological Survey of South Australia, Department for Energy and Mining, Adelaide 5000, SA, Australia

ARTICLE INFO

Keywords:

Receiver functions
Moho
Resonance filter
Gawler Craton
Proterozoic Australia

ABSTRACT

In this study, using two recent passive seismic deployments across the Gawler Craton and Lake Eyre Basin, South Australia, we aim to examine the nature and extent of a perceived Moho offset (~ 15 km) between the two regions using receiver functions. Together the two arrays straddle the edge of the Gawler Craton and present a unique opportunity to understand the crustal thickness variations in a hitherto under-explored region. The task is complicated however by many stations situated atop low-velocity sedimentary rocks, inducing high-amplitude low-frequency reverberations in the receiver function signal, and masking the signal from crust to mantle conversions. We, therefore, employed a resonance removal filter to dampen the sediment reverberation effect which aided the detection of the P-to-S conversion from the Moho. The obtained Moho depths dramatically increased the coverage in observations, particularly in areas inundated by Phanerozoic sediments. We detect the presence of thicker crust beneath the Lake Eyre region than previously imaged (~ 40 km), that hints towards a shared Proterozoic provenance with building blocks of the South Australian Craton, such as the Curnamona Province. The Moho phase is consistent (~ 46 km) and clear beneath the Gawler Craton, indicating a contrast with stations in the Lake Eyre region, although the difference with respect to previously reported crustal thickness is now substantially reduced. Our results thus illuminate the crustal structure of an important junction within continental Australia and provide valuable constraints for models of the tectonic evolution of eastern Gondwana and the assembly of Proterozoic Australia.

1. Introduction

It is well established that lateral changes in Moho depth (i.e. Moho topography) exist as a relic of past (and/or present) tectonic processes. Studying topographical variations of the Moho can therefore be crucial in understanding the large-scale processes that shape the Earth, such as orogenies or continental rifting (e.g. Eaton, 2006). On a more regional scale, short-wavelength changes in the Moho can identify the location of suture-zones or crustal-scale faults, structures which can provide potential pathways for fluids (e.g. Diaconescu et al., 1998; Wittlinger et al., 2004; Eaton, 2006; Wise and Thiel, 2020). The most prominent Moho offsets are usually ascribed to fault-systems in tectonically active areas such as Tibet (e.g. Wittlinger et al., 2004), the Alpine Fault in New Zealand (e.g. Stern and McBride, 1998), and the San Andreas Fault (e.g. Zhu, 2000). However, there are numerous examples of preservation of Moho topography in Precambrian suture zones, including the Canadian

shield, Baltic shield, Urals, and the Central Australia (Abramovitz et al., 1997; Diaconescu et al., 1998; Eaton, 2006; Sippl, 2016).

In Australia, geophysical methods are required to image the crustal structure as three-quarters of the surface is covered by a blanket of regolith. Methods such as active seismics, aeromagnetics, gravity, and magnetotellurics have helped map the crustal boundaries separating the different geological provinces and the crustal blocks that have been fused together to form the continent (e.g. Aitken et al., 2013; Korsch and Doublier, 2016). Seismic methods in particular, such as seismic reflection and refraction studies, as well as receiver function analysis from passive experiments, have been relied upon to determine the crustal thickness and map lateral variations of the Moho across the continent (Fig. 1c; Clitheroe et al., 2000; Collins et al., 2003; Kennett et al., 2011; Salmon et al., 2013; Kennett and Saygin, 2015; Kennett et al., 2016; Kennett et al., 2018). In addition, the autocorrelation technique has been useful in recovering P-wave reflectivity beneath seismic stations

* Corresponding author.

E-mail address: shubham.agrawal@anu.edu.au (S. Agrawal).

¹ Now at Geological Survey of Western Australia.

and inferring Moho depth (e.g. Gorbatov et al., 2013; Kennett and Saygin, 2015; Liang and Kennett, 2020). Most recently Qashqai et al. (2019) inverted autocorrelograms to map the Moho structure across Australia on a continental scale and retrieved patterns similar to previous crustal models such as AusMoho (Kennett et al., 2011; Salmon et al., 2013).

One area that has eluded both active and passive seismic experiments however is in central Australia in the region surrounding Kati Thanda-

Lake Eyre (KT-LE) and the Simpson Desert (white triangle in Fig. 1c). KT-LE represents the lowest point in Australia (15.2 metres below sea level) as well as the depocenter of the vast Lake Eyre Basin (Habbeck-Fardy and Nanson, 2014). This deserted region is mostly impassable by vehicle (except for a few unsealed tracks) and thus presents a significant gap in seismic network coverage. A limited number of measurements in the region suggested abnormally thin crust with Moho depths of 30 km or less (pale colours in Fig. 1a), indicating some of the thinnest imaged

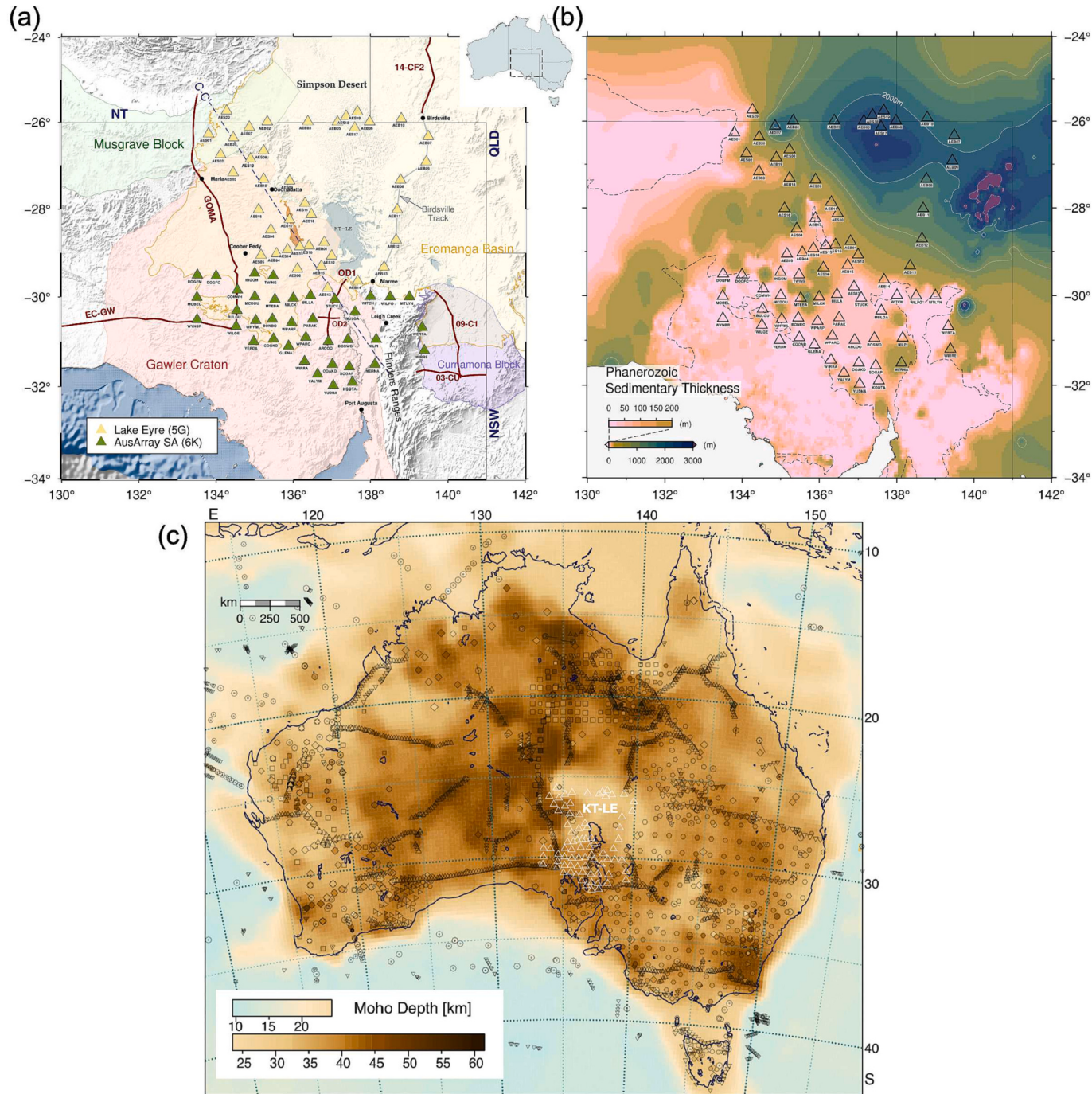


Fig. 1. a) Simplified geological map of the study region with seismic stations used in this study. The solid red lines denote the active seismic reflection profiles with their names printed in red (see Kennett et al., 2016, for an Australia wide compilation). The dashed blue line is the cross-section (C-C') used for receiver function stacking in Fig. 7. Outlines of the geological units are acquired from the Geoscience Australia database (Raymond et al., 2018) b) Interpolated map of Phanerozoic sedimentary thickness combining borehole measurements and receiver function based basement depth estimates from Agrawal et al. (2022). The contours are drawn every 1000 m as white lines, while the thin dashed black lines identify the geological provinces with little to no sediment cover. The colour bar is adjusted in the initial 200 km to reflect the sediment thickness variations. c) Interpolated Moho depth map for Australia modified after Kennett et al. (2018). The acronym KT-LE (Kati Thanda-Lake Eyre) denotes the region of perceived thin crust beneath the Lake Eyre region, with the stations used in the study superimposed as white triangles.

crust in Australia (Kennett et al., 2011). A short distance (~200 km) to the west, however, numerous active and passive seismic experiments have followed a north-south transect along the Stuart Highway (e.g. BILBY array). Along this profile, over the north-west Gawler Craton, some of the deepest Moho depths on the continent (> 50 km) have been identified (Kennett et al., 2011). This resulted in one of the sharpest estimated Moho offsets in the Australian continent, with a suggested difference in crustal thickness of at least 20 km separated in distance by only 200 km (Fig. 1c). To better understand the nature of this Moho offset, Liang and Kennett (2020) utilised a dense transect of 68 passive seismic stations deployed roughly every 3.5 km between the two regions, known as the Marla Line. Using autocorrelations they found evidence for a more gradual change in the Moho with a slightly thicker crust (35–40 km) for the easternmost stations (MAL 62–68) closest to KT-LE than previously estimated. Nonetheless the nature of the Moho beneath the broader Lake Eyre Basin and Simpson Desert remains poorly constrained by a small number of measurements, causing spatial discrepancies in crustal models of Australia (e.g. Kennett et al., 2011; Qashqai et al., 2019).

An additional complication for imaging the Moho in the region (and Australia in general) is the presence of thick sedimentary accumulations of up to 3000 m (Fig. 1b; Agrawal et al., 2022). In regions of Australia blanketed by sediments, the location of crustal boundaries becomes difficult to constrain (e.g. Korsch and Doublier, 2016), as gravity and magnetic crustal anomalies become more diffuse and the energy from seismic waves become trapped in sedimentary basins. The north-east corner of South Australia beneath the Lake Eyre Basin and Simpson Desert is one such heavily sedimented region, where it has been difficult to identify crustal boundaries from potential field methods (e.g. gravity). The addition of targeted seismic deployments can help determine sub-surface crustal discontinuities. One of the most common approaches to determine the Moho depth beneath a seismic station is from receiver functions (RF) which detect seismic wave (P and S wave) conversions manifested by wave-speed discontinuities (Langston, 1979; Vinnik, 1977). In the presence of unconsolidated sediments, however, receiver functions are contaminated by strong reverberations due to the significant impedance contrast between the basement rock and the low-velocity sedimentary layer which traps the seismic waves creating a significant resonance effect (e.g. Zelt and Ellis, 1999). This can last for a few seconds after the direct-P arrival and mask the signal from deeper crustal discontinuities such as the Moho (e.g. Zelt and Ellis, 1999; Clitheroe et al., 2000; Yeck et al., 2013; Srinivas et al., 2013; Tao et al., 2014; Agostinetti et al., 2018; Cunningham and Lekic, 2019; Zhang and Olugboji, 2021). Therefore, it is essential in sedimented areas that the reverberation energy is removed/reduced before attempting to interpret the Moho on receiver functions.

In this study, we aim to characterise the nature of the Moho beneath Lake Eyre Basin and the eastern Gawler Craton in central Australia by applying receiver function analysis to two recently completed seismic deployments; the Lake Eyre Basin Array and the AusArray-SA (triangles Fig. 1a). We investigate the extent of the proposed abnormally thin crust beneath Lake Eyre Basin, as well as, any crustal variations associated with the internal structure of the craton and its margin. Following on from our previous work to characterise the depth of sedimentation across South Australia (Fig. 1b; Agrawal et al., 2022), we carefully consider the influence of varying amounts of sediment on the quality of the receiver functions and apply a resonance removal filter (Yu et al., 2015) to suppress the S-wave sediment reverberations that improves Moho detection.

2. Geological and crustal architecture

The western two-thirds of Australia is of Precambrian origin hosting several Archean cratons such as the Yilgarn, Pilbara, and Gawler Cratons (e.g. Betts et al., 2002; Cawood and Korsch, 2008). In comparison the eastern third of Australia was accreted via subduction during the

Cambrian to Triassic (~550–220 Ma) as a series of orogenic belts, collectively known as the Tasmanides (e.g. Glen, 2005; Glen, 2013; Rosenbaum, 2018). The elusive boundary demarcating the western Proterozoic versus eastern Phanerozoic Australia is sometimes referred to as the Tasman line (e.g. Direen and Crawford, 2003, for a detailed discussion). Originally, the term was introduced based on rock outcrop - to describe an approximately rectilinear junction between Precambrian and early Palaeozoic rocks in the Mt Isa block in Queensland. Since then, the term has been attributed to various tectonic scenarios such as the Rodinian rifted margin, the western limit of deformation (suture) of the Tasman Foldbelt System, or a Proterozoic continental boundary, with studies adjusting the position, character, and age of the proposed line based upon their hypothesis (Direen and Crawford, 2003).

The most widespread technique to try to identify the Tasman Line is through overlapping magnetic and gravity lineaments; however, the position of the Tasman Line is essentially unconstrained and varies between studies where magnetic and gravity anomalies have a broader wavelength (often in heavily sedimented areas). One such place is in the north-eastern corner of South Australia bordering New South Wales where there is significant Phanerozoic sedimentary cover, as is readily illustrated by Fig. 1b. Overlapping sedimentary rocks from the Paleozoic Warburton Basin, Palaeozoic-Mesozoic Cooper Basin, Mesozoic Eromanga Basin, and the Cenozoic Lake Eyre Basin obscure the basement rocks below. Some authors have included this region in Phanerozoic Australia, i.e. placing the Tasman Line to the west coincident with the north-east margin of the Gawler Craton (e.g. Shaw et al., 1995; Glen, 2005; Glen, 2013; Spampinato et al., 2015). Depictions of the crustal boundaries within Australia often assign then the Lake Eyre region to the Delamerian and Thomson Orogenes (i.e. part of the Tasmanides reworked during the middle-late Cambrian Delamerian Orogeny), but with low to zero confidence on the position of the boundaries (e.g. Glen, 2013; Korsch and Doublier, 2016). Others have speculated that the oldest Phanerozoic basin in the region - Warburton Basin – is underlain by Proterozoic basement (e.g. Gatehouse, 1986; Meixner et al., 2000); however, the nature and age of the crust beneath this region still remains elusive (e.g. Rosenbaum, 2018; Abdullah et al., 2019).

To the south and southwest of this region of obscured crustal basement, lies the Curnamona Province and Gawler Craton (Fig. 1a), which together form the core of the South Australian Craton (e.g. Hand et al., 2007; Cawood and Korsch, 2008). The Gawler Craton is the oldest and largest geological province in South Australia and preserves a complex tectonic history spanning between 3200 Ma and 1450 Ma (e.g. Myers, 1990), containing some of the oldest rocks found in Australia (≥ 3.1 Ga; Fraser et al., 2010). The Archaean and Paleoproterozoic core of the Gawler Craton forms a folded belt around an apparent orocline as it underwent deformation along discrete shear zones during the Mesoproterozoic (Hand et al., 2007). During the Proterozoic, the region saw multiple major magmatic events, namely, Donington Suite (ca. 1850 Ma), St. Peter Suite (1620 to 1610 Ma), and Gawler Range Volcanics-Hiltaba Suite (1595 to 1575 Ma; Hand et al., 2007). In addition, the eastern margin of Gawler Craton hosts significant iron oxide-copper-gold deposits, including the world-class Olympic Dam, while the central Gawler Craton has Au-dominant deposits (see Reid, 2019, for a recent review). Both zones of mineralizations are thought to be early Mesoproterozoic, coeval with extensive magmatism (e.g. Gawler range volcanic and Hiltaba suite) and crustal deformation (Skirrow et al., 2007).

Further north of the Gawler Craton lies the Musgrave Province, composed of high-grade Mesoproterozoic to Neoproterozoic metamorphic rocks (Wade et al., 2008). The most recent intra-cratonic activity in the region was the high-strain, low-temperature Petermann orogeny (570–530 Ma), which resulted in the current east–west dominated architectural structure of the Musgrave Province and present-day Moho geometry (e.g. Major and Conor, 1993).

To the southeast, the Gawler Craton is bounded by the Neoproterozoic Adelaide Superbasin (previously referred to as Adelaide

geosyncline or Adelaide fold belt), encompassing the Flinders Ranges. The Adelaide Superbasin incorporates a series of rift and sag basins, possibly related to break-up of Rodinia (e.g. Betts et al., 2002). The crystalline basement in the Superbasin resembles portions of both the Gawler Craton and Curnamona Province in age and composition, supporting the interpretation that they once were juxtaposed (Preiss, 2000). The northern extent of this geological province however is less well constrained due to increasing overlying sedimentation. Lloyd et al. (2020) suggested a possible northern extension of the Superbasin based on rocks obtained from two boreholes. However, the lack of outcropping rock at the surface hinders further insight into the nature of the underlying crust.

3. Data & methods

3.1. Seismic data coverage

Due to the remoteness and inhospitality of the Australian continental interior, the seismic data coverage is non-uniform and restricted by the available transportation routes, such as the limited locations of unsealed (i.e. dirt) tracks. Many gaps or blind spots in seismic coverage still exist, such as that surrounding Kati Thanda-Lake Eyre (KT-LE). To help increase the coverage in South Australia, the Lake Eyre Basin array (Eakin, 2019) consisting of 40 seismometers (both short-period and broadband) was deployed encircling KT-LE (yellow stations in Fig. 1a). Stations were deployed in approximately three transects following available routes, such as the Birdsville Track (annotated in Fig. 1a) to the east of KT-LE, and the Oodnadatta Track to the west. To the north, along the border between South Australia and the Northern Territory, stations were deployed in the Simpson Desert for the first time (made only possible by helicopter). An initial deployment of a sub-set of stations started in September 2018, and the full array was in place by October 2019. The array was decommissioned in July 2022. Installation and servicing of the deployment was impacted at various times by flooding (making access tracks impassable) and state border restrictions during the COVID-19 pandemic. Significant periods without data include March–July 2019 and June–October 2020.

A contemporaneous passive seismic experiment titled AusArray-SA (green stations in Fig. 1a) operated by the Geological Survey of South Australia deployed 38 seismic stations across the eastern Gawler Craton (O'Donnell et al., 2020a,b). The array substantially improved the coverage within the craton, and operated from October 2020 to June 2022. Together the two arrays straddle the edge of the Gawler Craton and present a unique opportunity to better understand the crustal variations across the region.

3.2. Methodology

3.2.1. Receiver function calculation

Receiver functions are a common passive-seismic technique to estimate the Moho depth, in which seismic wave (P and S wave) conversions arising from the wave-speed discontinuities are detected (Langston, 1979; Vinnik, 1977). The near-receiver structural response can be estimated from the three-component seismogram of teleseismic earthquakes by removing the contribution from the source and wavefield propagation. This is achieved by deconvolving the vertical component of the seismogram from the horizontal to obtain the radial receiver functions (RFs) (Langston, 1979; Vinnik, 1977; Ammon, 1991; Ligorría and Ammon, 1999).

In this study, the *rf* python package (Eulenfeld, 2020) was used for all the receiver function analyses. For each station, earthquakes with magnitude ≥ 5.5 and in the distance range $35\text{--}95^\circ$ were acquired, and events with a signal-to-noise ratio less than 1.5 were discarded. The 100 s long seismograms (25 s before and 75 s after the P wave arrival) were bandpass filtered between 0.1–1 Hz, demeaned, de-trended (linear), and cosine tapered. The radial receiver functions were calculated using an

iterative time-domain deconvolution (Ligorría and Ammon, 1999), to maintain consistency with our previous study (Agrawal et al., 2022). An attempt was made to also calculate the transverse component receiver functions for these stations but due to their complexity they did not prove useful (Fig. S1). RFs were then corrected for different slowness by applying a moveout correction such that all resulting traces had the same reference slowness of 6.4s^{-1} . It was also ensured that the largest arrival on the radial RF was a positive polarity peak arriving within 2 s of the direct P, to remove spurious and unstably deconvolved RF.

3.2.2. The influence and removal of sediment reverberations on receiver functions

Our study area in South Australia is known to include varying degrees of sedimentation (Fig. 1b). As such we inspected the character of the receiver functions from all stations to assess the influence of the sediments, and how our ability to detect the Moho might vary with sediment thickness. Agrawal et al. (2022) described in detail the different ways RFs are influenced by the presence of sediments in South Australia. The common attribute is a delay in the direct P phase on the radial RF due to its conversion into an S phase at the sediment–basement boundary, henceforth referred to as the PS_b phase (annotated in Fig. 3a). RFs in Fig. 2 are arranged in increasing order of the PS_b arrival (referred to as dt), with the highest delay of 1.32 s for station AES18. Another common characteristic is the presence of reverberatory signal that can last up to several seconds, as is evident in Fig. 2 (for example, stations AEB15, AES02, AEB13). The reverberations result from the S phase trapped in the sediment layers due to an impedance contrast between the sediment layers and the basement rock (Fig. 3a). However, in the presence of multiple or thick sedimentary layers, the RF gets further complicated. Overall RFs showed signs of being affected by sediments for all stations from the Lake Eyre array except for three. In contrast for the AusArray-SA network, only eight stations showed influence of sediments.

Numerous methods have been employed by previous studies to aid detection of the deeper crustal structure from RF in the presence of low velocity sediments (Langston, 2011; Leahy et al., 2012; Yeck et al., 2013; Tao et al., 2014; Yu et al., 2015; Parker et al., 2016; Cunningham and Lekic, 2019; Zhang et al., 2019; Wang et al., 2020). As an alternative to correcting for the sediment effects, some studies have attempted to forward model the crustal and sediment structure (e.g. Clitheroe et al., 2000). However, this method is computationally intensive, especially in the presence of sediments, due to the large number of parameters that need to be considered. Further, there is a fundamental problem of non-uniqueness in the solution. A more efficient method to determine the seismic velocity structure and Moho depth would be to do a joint inversion of receiver functions and surface waves dispersions, which can better constrain the underlying crustal and sediment structure (e.g. Julia et al., 2000; Bodin et al., 2012). In this study, our primary focus is on obtaining initial estimates of the Moho depth and therefore, we adopt the methodology of Yu et al. (2015) to suppress the S-wave sediment reverberations, which uses a resonance removal filter based on the autocorrelation of the radial RF. Yu et al. (2015) observed that the S phases reverberations (reverberatory phases in Fig. 3a) trapped in the low-velocity sedimentary layer are similar to the multiples created in water and therefore, their signature can be predicted/modelled. A sedimentary layer also has a fundamental resonant frequency for the S reverberations, which is inversely proportional to the two-way travel time of the S leg in the sediment layer (e.g. Cunningham and Lekic, 2019). Thus, an appropriate resonant filter can be constructed using the relative strength of the reverberation (r_0) and the two-way travel time of S phase in the sediment layer (Δt).

Although the two parameters, r_0 and Δt described above, can be read directly from the radial RF, they are routinely determined from the autocorrelation function of the receiver function. As illustrated in Fig. 3b, r_0 and Δt , are respectively the amplitude and the arrival time of the first negative peak in the autocorrelation function. Both these

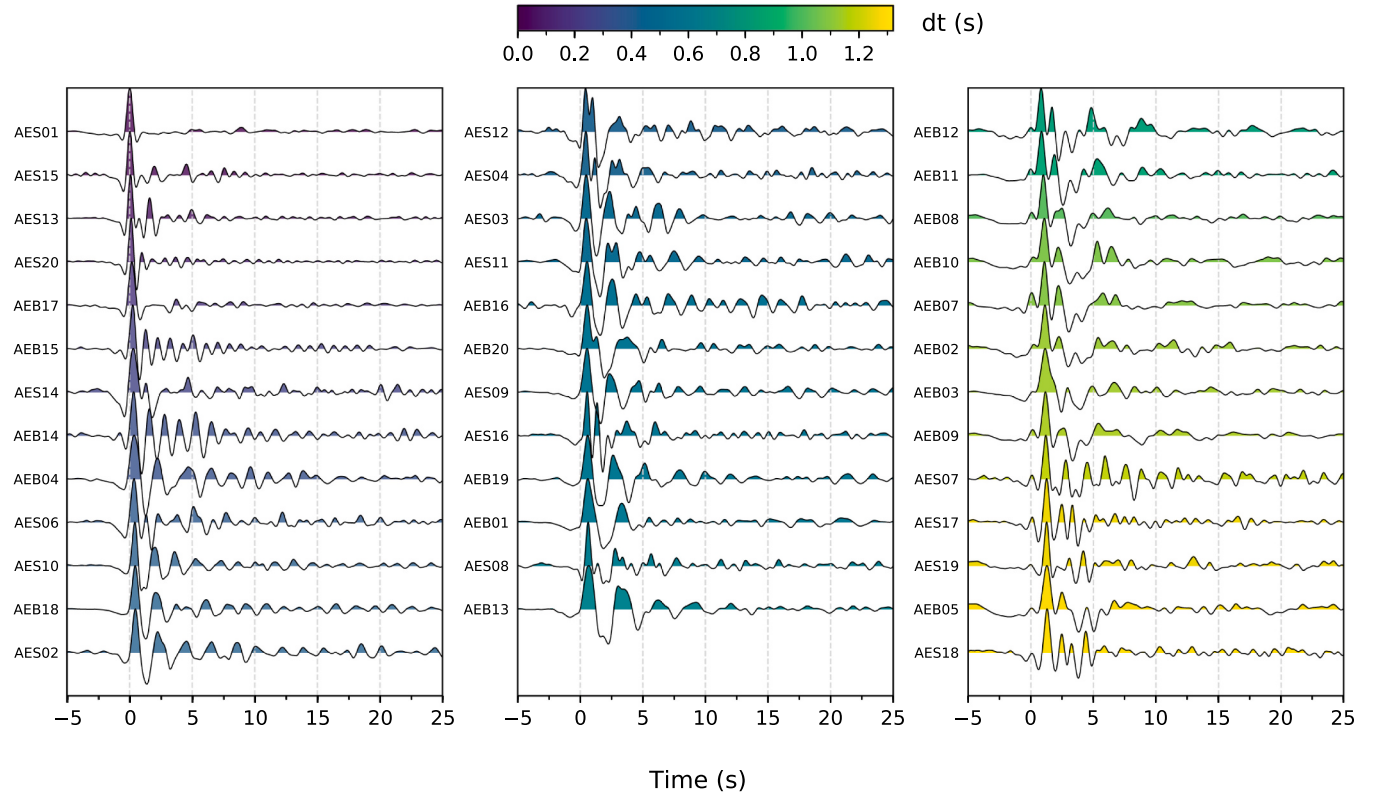


Fig. 2. Receiver function stacks for stations from the Lake Eyre Basin array arranged and coloured by the arrival time of the P converted to S phase (dt) at the crust-sediment boundary. The character of the receiver function changes as the sediment thickness increases, from top left to bottom right. In the first two columns, the customary sinusoidal reverberations can be observed, best seen in stations AEB15, AES02, and AEB13. However, this behaviour diminishes with an increase in sedimentary thickness, as seen in the third column.

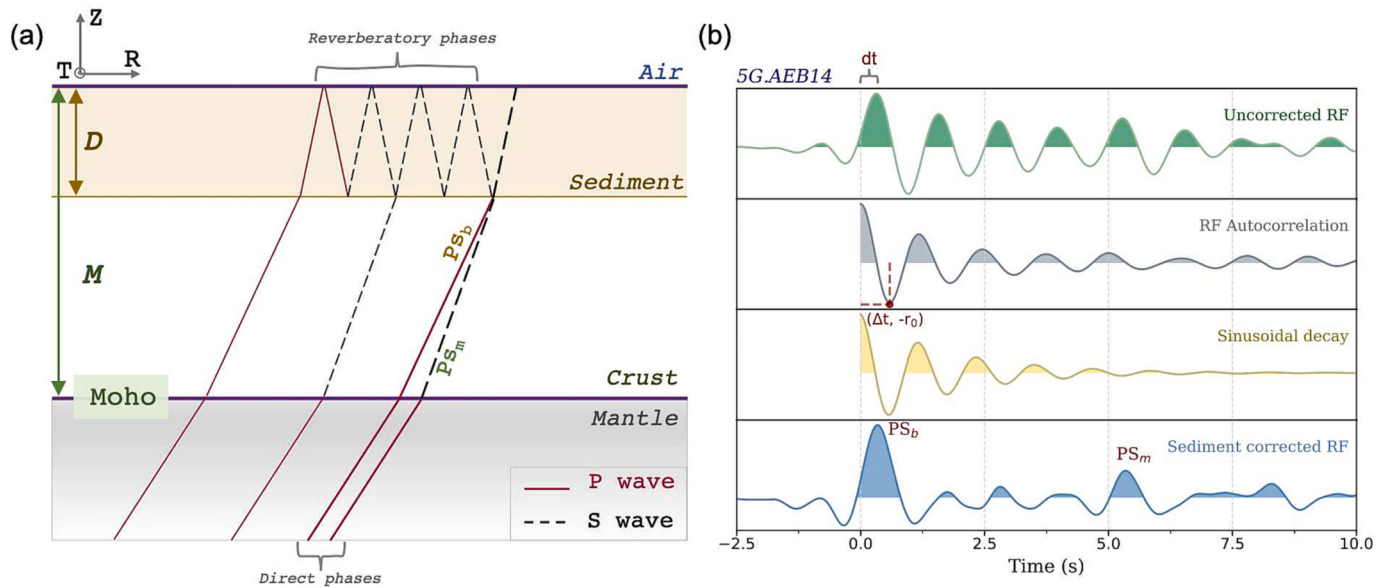


Fig. 3. a) Illustrative ray paths showing the conversions at the crust-mantle and the sediment-crust boundaries. The rays are classified as direct (thicker lines) and reverberatory (thinner lines) based on their respective paths through the sediment layer (shaded yellow). Note the figure is illustrative and not to scale. b) An example of the process of constructing and applying the resonance filter (Yu et al., 2015) for a single receiver function for station AEB14 (green). In the uncorrected RF, dt marks the delayed arrival of the Ps_b phase with respect to direct P. Autocorrelation of the uncorrected RF is shown in the second panel, where r_0 and Δt indicate the strength of the sedimentary reverberations and the two-wave S travel time in the sediment layer, respectively. These parameters are used to construct the best-fitting decaying sinusoid from the autocorrelation function (yellow) shown in the third panel. The corrected RF signal obtained after the application of the resonance removal filter (blue) allows for a clearer identification of the P-to-S conversion from the Moho (PS_m).

parameters are calculated for each individual RF as often the reverberation signature can be different for different backazimuths. Another benefit of applying the resonance filter individually to each trace is it allows us to monitor the automatically picked r_0 and Δt values from the autocorrelations. As shown in Fig. S2a for station AES08, for some events, the Δt values are anomalously larger or smaller; thus, placing some theoretical constraints on Δt values can help regulate the resonance filter efficiency.

From Fig. 3, both dt and Δt can be expressed as

$$dt = D \left(\frac{1}{V_{sedi}} - \frac{1}{V_{p_{sedi}}} \right) \quad (1)$$

$$\Delta t = \frac{2D}{V_{sedi}}, \quad (2)$$

where D is the total thickness of the Phanerozoic sediments and $V_{p_{sedi}}$ & V_{sedi} are seismic velocities in the sediment layer. From the above two equations, dt and Δt are related as,

$$\Delta t = 2dt + \frac{2D}{V_{p_{sedi}}}. \quad (3)$$

Therefore,

$$\Delta t \geq 2dt. \quad (4)$$

We used this relationship to remove RFs with low Δt values smaller than $2dt$. Although the lower limit of Δt is useful, it is more difficult to

establish an upper limit. Therefore, we individually pick the upper bound for each station based on the overall character of the autocorrelations. An example is shown in Fig. S2 where only autocorrelations with $2 \geq \Delta t \geq 1$ were kept, thus removing RFs with unreasonable values of Δt , which also served as an additional quality filter.

Since this method assumes a sinusoidal sediment reverberation behaviour, it works best when the reverberations have a single dominant frequency. As could be observed in RF stacks in the third column of Fig. 2, for stations with dt values greater than 0.8 s (equivalent to sediment thickness ~ 800 m or more), no single dominant frequency can be observed; thus, a resonance filter will be inadequate in replicating the sediment reverberations. Therefore, in such cases, the resonance filter was not applied. An example of the constructed resonance filter, or in other words the decaying sinusoidal, for station AEB14 is shown in Fig. 3b. The corrected RF are obtained by convolving the resonance filter by the radial RF in the frequency domain, resulting in the corrected RF (blue RF in Fig. 3b).

3.2.3. Determining the phase arrival and estimated depth of the Moho

Even after applying the reverberation correction, the Moho converted S phase, hereafter denoted as the PS_m pulse, was often fairly weak or had pronounced backazimuthal variations. Consequently, the Moho multiples (PPS_m and PSS_m) were significantly harder to observe on the RFs, challenging the use of methods such as H- κ grid search (Zhu and Kanamori, 2000). Despite the sediment corrections, the Moho depths obtained using modified H- κ (Eq.(5) of Yu et al., 2015) were largely unconstrained (Fig. S3). Therefore, the PS_m pulse was picked

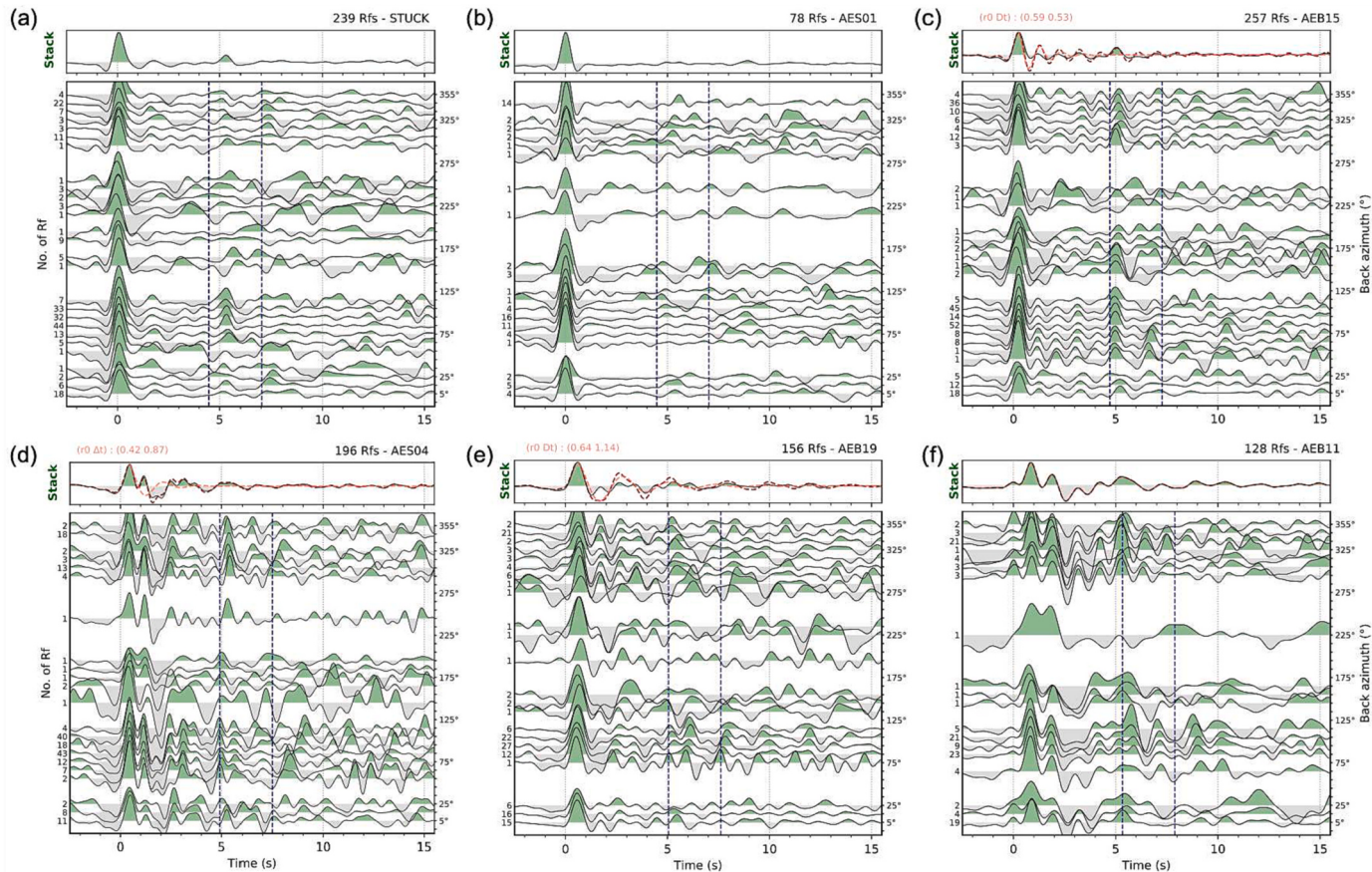


Fig. 4. Six representative stations showing the various character of the receiver functions across the study region. For all cases, the receiver functions are displayed as stacks in 10° backazimuthal bins with the top panel showing the full station stack. The dashed blue lines indicate the expected arrival of the PS_m pulse for Moho depths of 35 km and 55 km, with the arrival time adjusted for the delay in the presence of sediments. The top panel also displays orange and red dashed lines, which are the decaying sinusoidal filter and the uncorrected receiver function (see Fig. 3b). Printed in orange at the top are the resonance filter parameters, r_0 and Δt , where applicable.

individually for all stations using RF stacked in each 10° bin. This step facilitated the PS_m picking without hiding the backazimuthal variability (Fig. 4). The expected arrival of PS_m (corrected for sediments; Eq. (5) of Yu et al., 2015) for Moho depths 35 km and 50 km were plotted as dashed blue lines to aid the identification of the PS_m pulse.

To ensure consistency in manual picking of the PS_m phase, we followed the following criteria: a) in most cases, PS_m was the largest amplitude positive peak in the expected time-window; b) a coherent and similar shaped PS_m pulse was sought that could be traced across the backazimuthal bins (e.g. Fig. 4b); c) bins with a larger number of RFs and a clear PS_m pulse had a greater influence on the final picks than bins with smaller number of events.

Although the PS_m phase is more clearly observed on the RFs after applying the resonance filter, the S phase still travels through the low-velocity sediment layer, accruing a time delay, which needs to be adjusted. This delay is equivalent to the arrival time of the PS_b phase, i.e. dt (Fig. 3), which is the first large positive arrival on the RF, and thus is easily measured. This value is then subtracted from the PS_m time to determine the travel time associated only with variations in crustal thickness rather than sediment.

The corrected PS_m time was converted to depth using an Australia wide 3D crustal velocity model (AusREM; Salmon et al., 2013). A regional 1D V_p - V_s velocity was obtained by averaging the AusREM model for the region of interest, i.e., the area encompassing both arrays (Fig. S5). The time to depth conversion provides an estimate of the crustal thickness beneath each station (not including the overlying sediments). To obtain a Moho depth for comparison with other studies, the sediment thickness values from Agrawal et al. (2022) are added back.

3.2.4. Estimation of the Moho depth uncertainty

The methodology and the subsequently obtained Moho depths in this study have some inherent uncertainties. The resonance removal filter does not always work as intended and there might be residual sediment reverberation energy in the receiver function (discussed in detail in next section). For some stations, PS_m pulse showed backazimuthal variations up to 0.4 s. In such cases, we picked an average PS_m time, thus we attribute an error of ± 0.2 s owing to manual pulse picking. When the backazimuthal variations were more prominent, we picked two Moho pulses. We then subtracted PS_b arrival time (dt) from the PS_m time to remove the delay due to slow velocities in the sediments. Agrawal et al. (2022) discussed the uncertainties in dt values arising from - but not limited to - frequency dependence, and they prescribed an error of ± 0.125 s in dt values. Then, we used an Australia wide 3-D velocity model (AusREM; Salmon et al., 2013) to extract average crustal velocities for the study region, and consequently, a conversion factor of 8.9 was used to convert the obtained time ($PS_m - PS_b$) to depths (Fig. S5). Using a global 1-D velocity model (IASP91; Kennett and Engdahl, 1991) resulted in a conversion factor of 9, whereas the average Crust1.0 velocity model (Laske et al., 2013) indicated a conversion factor of 8.95. Thus, we have attributed an error margin of ± 0.1 to the conversion factor, as it is based on the greater deviation from AusREM. And lastly, we added the Phanerozoic sedimentary thickness (errors of ± 360 m; Agrawal et al., 2022) to the crustal thickness to estimate the final Moho depths. The final equation, with errors, is of the form,

$$M(km) = (\alpha \pm 0.1)(PS_m \pm 0.2 - PS_b \pm 0.125) + (D \pm 0.360), \quad (5)$$

where α is the time-to-depth conversion factor and the rest are the same as in Fig. 3a. Propagating the errors in the above equation results in estimated Moho depth errors of ± 3.50 km. The magnitude of the expected error is important to keep in mind when considering the results in the following sections. Furthermore, we recognize that the adopted approach to obtain the initial estimate of the Moho depth is non-standard. While it would be preferable to explore the parameter space by inverting for both crustal and sedimentary properties, at present

there are no local velocity models yet available to help constrain such modelling. To address this, once further studies have been conducted, we plan to use a joint inversion of receiver functions and surface waves for a more comprehensive analysis in the future.

4. Results

4.1. Improvements and limitations of applying the resonance filter

The sediment corrected RFs stacks for both Lake Eyre Basin and AusArray-SA arrays are depicted as blue lines in Fig. 5a, along with the uncorrected RFs (yellow lines). Only stations where the resonance filter was applied are shown (located on less than ~ 800 m sediment). For most cases, the filter works as intended, suppressing the reverberations and thus, in effect magnifying the P to S conversion from the Moho (PS_m).

The reverberation filter parameters - r_0 and Δt - were most efficiently read from the autocorrelation of the radial RF, as suggested by previous studies (e.g. Yu et al., 2015; Cunningham and Lekic, 2019). The decaying sinusoids obtained using the autocorrelation are shown in Fig. 5b, with the r_0 and Δt printed for each station. However, we observed that for most stations, r_0 and Δt values varied considerably between individual traces (Fig. S2c). This may be due to multiple sedimentary basins resulting in multiple minimas in auto-correlations (e.g. Cunningham and Lekic, 2019). Therefore, checking the r_0 and Δt values for each station proved pivotal before applying the resonance filter.

As indicated in Eq. (4), dt and Δt are related, as both depend on the travel time of the S-phase in the sediment layer (Fig. 3). However, the upper bound on Δt is more difficult to constrain; therefore, we visually inspected the autocorrelations and determined the upper limit individually for each station. Removing traces with Δt values outside the limits thus brought down the standard deviation of the parameters significantly (Fig. S2c) and therefore worked as an additional quality check. Further, given the backazimuthal variations, the amplitude of reverberations (r_0) was found to vary, thus, applying the resonance filter to each trace helped ensure the filter's efficiency.

For stations with thick sediments underneath, the RFs become more complicated with multiple resonant frequencies present (e.g. yellow to green RFs in Fig. 2). Resonance filters constructed from the autocorrelations of such RFs were found to have low r_0 values (i.e. lower amplitude) due to lack of a single dominant reverberatory frequency in the RF. The efficacy of the resonance filter is therefore reduced, despite the presence of thick sedimentary sequences. Further, for such cases, regulating the Δt values from the autocorrelations is significantly more tricky. Fig. S2b shows the autocorrelations for station AES17 located on thick sediments. As is evident, there are multiple local minimas, and having no upper limit on Δt makes it difficult to reliably remove outliers.

For some stations (AEB01, AES02, AES03, NILPI, and MERNA), the resonance filter was unable to satisfactorily remove the reverberatory energy, thus we chose to exclude such cases from the analysis (white circles in Fig. 6). Even though the filter parameters - r_0 and Δt - were consistent between the traces, it is evident from Fig. 5b that for these stations, the sinusoidal decay filter is lagging the RF, resulting in inaccurate removal of reverberation energy. Thus it was important to individually check RFs post sediment correction to ensure the effectuality of the filter.

For most of the stations, the decaying sinusoidal filter amplitude is most prominent in the first 4 s (Fig. 5b), reducing the sediment reverberation energy before the expected arrival of the PS_m pulse. For cases with very thin sediments, the filter amplitude (r_0) is small, resulting in the quick decay of the sinusoidal filter and thus not affecting the RF after 2.5s. The increase in sediment thickness (the RFs are arranged in increasing order of PS_b arrival or dt value), is reflected by a steady increase in both r_0 and Δt values (see also Fig. S4).

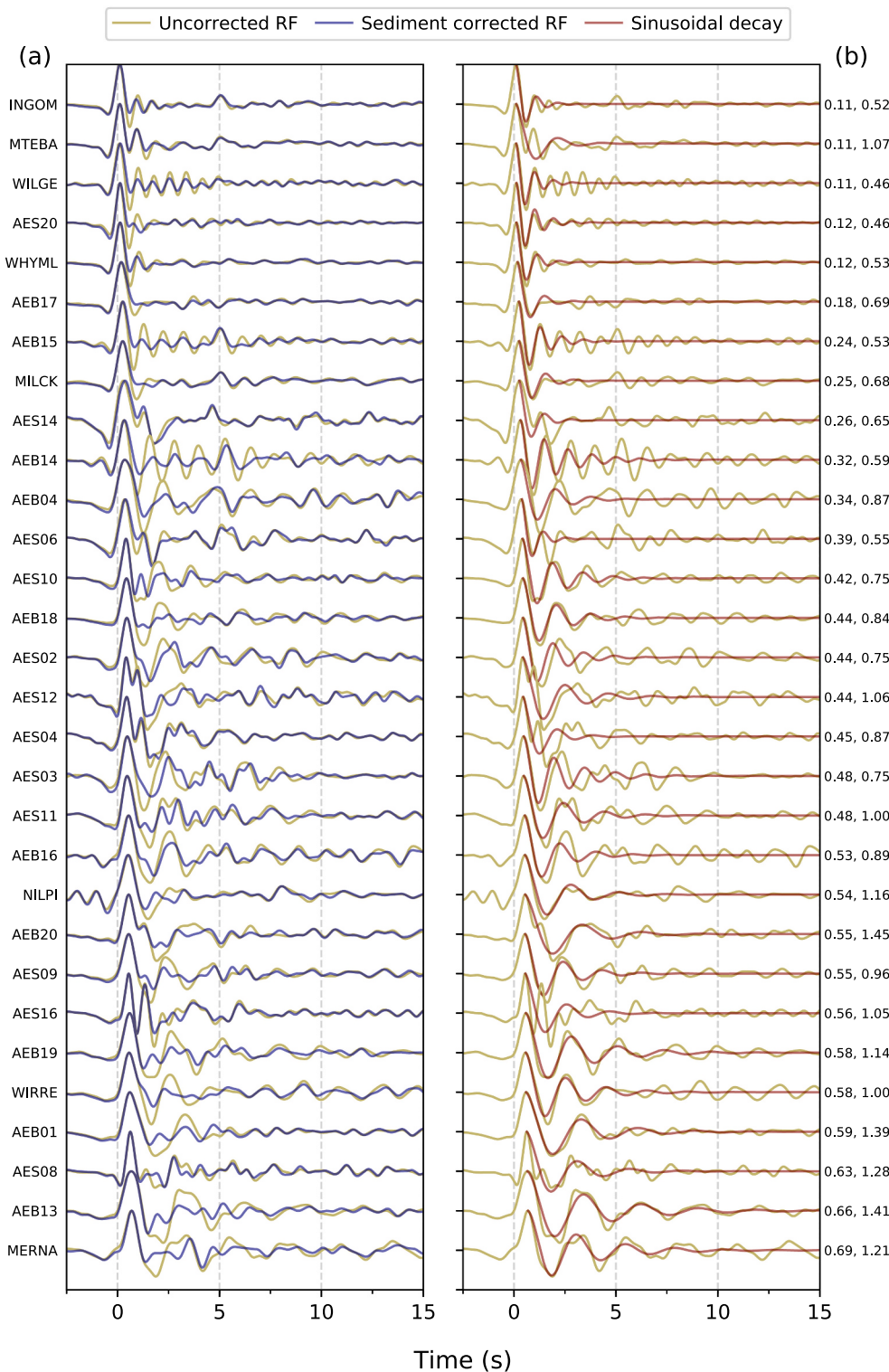


Fig. 5. a) Receiver functions stacks before (yellow) and after (blue) applying the resonance filter for stations with expected sedimentary thickness <800 m. b) The decaying sinusoid generated for each station (red line) constructed using the autocorrelation properties of the receiver functions (Fig. 3b). For visualisation purposes, the sinusoid is shifted on the time axis by Δt to align with the uncorrected receiver function. The mean r_0 and Δt values (resonance filter parameters) for each station are printed on the right.

4.2. Character of the receiver functions and identification of the PS_m phase

After applying the resonance filter and correcting for sediments, a perceptible PS_m pick was observed for 73 stations (out of 78 total (Table S1)). Overall, the stations from AusArray-SA located on the Gawler Craton had a much clearer Moho pulse compared to stations from the Lake Eyre Basin array which are situated on varying amounts of

sediment (Fig. 1). The PS_m pulse showed significant variations between stations reflecting varying sedimentary and crustal signatures.

Fig. 4 shows representative cases of the RF behaviour observed across the two arrays. For many stations from AusArray-SA, an unmistakable PS_m pulse, such as station STUCK (Fig. 4a), was recognised, with little to no variation in PS_m arrival for different backazimuths. However, there were stations such as AES01 (Fig. 4b) that had a feeble PS_m pulse suggestive of a transitional Moho. Two groups of such stations were

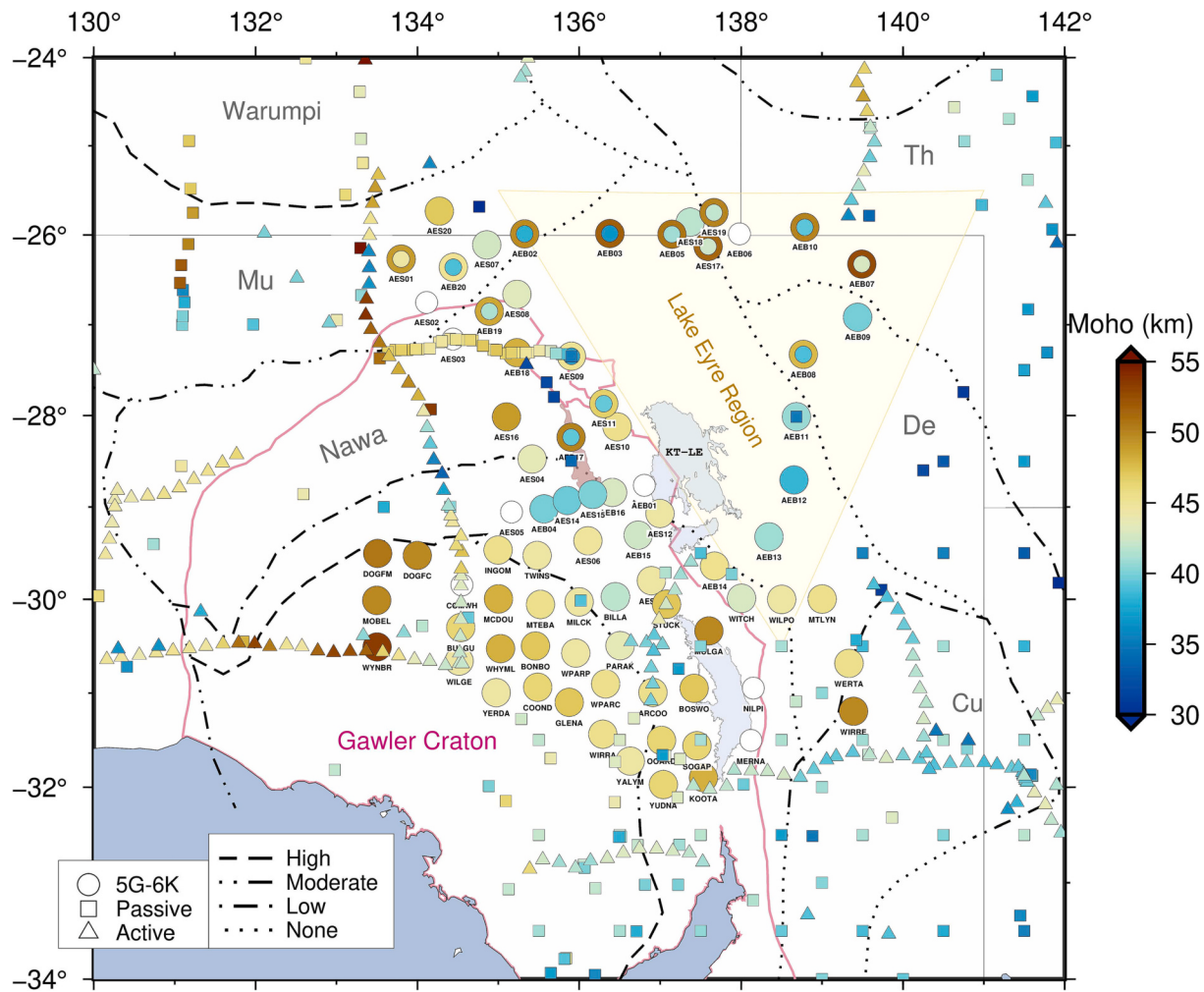


Fig. 6. Obtained Moho depths for Lake Eyre and AusArray SA stations displayed as coloured circles. Concentric circles are drawn for stations where two PS_m pulses were identified, with the shallower estimate being the inner circle. Also shown are previous Moho estimates across the region from active and passive seismic methods, depicted as square and triangles, respectively (Kennett et al., 2011; Salmon et al., 2013; Kennett et al., 2018). Dotted and dashed grey lines show the inferred crustal boundaries from Korsch and Doublier (2016), with varying degrees of confidence as indicated in the legend. Solid pink line denotes the inferred continental boundary of the Gawler Craton (<https://map.sarig.sa.gov.au/>). KT-LE - Kati Thanda-Lake Eyre, Mu - Musgrave Province, Th - Thomson Orogen, De - Delamerian Orogen, Cu - Curnamona Block. Shaded yellow triangle represents the area denoted as the Lake Eyre Region in Fig. 10.

identified; one group situated on the Warumpi Province and the other on the Peak and Denison Inlier. Examples of where the resonance filter worked efficiently are shown in Fig. 4c-d for stations AEB15 and AEB18, even though the reverberatory signature is quite different in both cases.

For stations such as AEB19 (Fig. 4e), there were two indistinguishable peaks within the predicted arrival window of the PS_m pulse (i.e. between the two dashed blue lines). In total, 13 such stations were recognised and thus both picks were included in the analysis (indicated by inner and outer circles in Fig. 6). The two pulses may be either indicative of two impedance contrasts associated with the transition from crust to mantle, indistinguishable PS_m and reverberatory phases, or the possible presence of crustal faults. In the last example (Fig. 4f), for stations located on thick sediments (>800 m), the PS_m pulse was the most challenging to identify as a sediment correction is ineffective for such stations. AEB11 is one such station; despite the high amplitude sediment-related noise in the RFs, a prominent and coherent positive PS_m pulse can still be detected around the 5.5 s time stamp that is most likely associated with the conversion at the Moho.

4.3. Moho spatial patterns

Fig. 6 displays the Moho depth variations for the two arrays, plotted

as coloured circles. Stations from the Lake Eyre Basin array reflect a rather complicated Moho topography (mean: 43.50 km; standard deviation: 4.40 km), with variation both N-S trending (alternating brown to light blue colours on the western side of the array) and E-W trending (i.e. shallower Moho indicated by blue colours on the eastern side of the array). In contrast, for AusArray-SA stations located over the Gawler Craton, Moho depths are spatially more consistent and deeper (mean: 46.20 km; standard deviation: 2.50 km). For most AusArray-SA stations, a clear and strong PS_m pulse was identifiable (e.g. Fig. 4a).

For stations with two Moho values, the inner circle corresponds to the shallower PS_m pick. For the 36 Lake Eyre array stations where a Moho pulse was identified, 13 stations registered a double PS_m pick. An advantage of plotting both prospective Moho pulse is it allows for scrutinising possible reasons for Moho variations within a region and helps discern the similarities between stations located in geographical vicinity. For example, stations with a double PS_m pick across the stations the Simpson Desert and Lake Eyre Region (yellow shading Fig. 6) showcase very similar Moho behaviour for both shallower (39–42 km) and deeper estimates (47–53 km), with the shallower values matching the nearby seismic reflection line estimate (36 km; 14-CF2 in Fig. 1a). Several stations on and adjacent to the Musgrave Province also display double Moho picks but with considerable variation, and could be related

to the uplifted crust of the Musgrave Province and associated crustal scale faults (Korsch et al., 2010a). Another sub-group of double PS_m picks are associated with the Paleoproterozoic-Ordovician Peake and Denison Inlier (red shaded area in Fig. 6), wherein the crustal thickness is about 5 km shallower than on either side of the inlier. This is further reinforced in individual RFs for stations AES16 and AES04 (Fig. 4d) which display a shallower Moho for eastern backazimuths (towards the inlier) compared to northern backazimuths.

The thickest crust for the entire study area was found under station WYNBR (53.50 km), at the western extent of the AusArray-SA array within the interior of Gawler Craton (drawn as a solid pink line in Fig. 6). The stations north of WYNBR (MOBEL, DOGFC, and DOGFM) also recorded crustal thicknesses of more than 50 km, confirming the presence of thicker crust within the interior of Gawler Craton, with a similar character seen in the EC-GW seismic reflection profile (Fig. S6b). On the other hand, some of the shallowest Moho depths were observed for stations situated north and east of KT-LE, along the Birdsville Track and across the Simpson Desert (average Moho depths of ~40 km). Comparing these relatively shallow Moho depths to the stations within Gawler Craton where the average Moho depth is around 45 km, the transition from Gawler Craton to the Lake Eyre Region therefore seems to be gradual, rather than an abrupt change, as previously interpreted (Kennett et al., 2011; Salmon et al., 2013). Along the interpreted eastern boundary of the Gawler Craton (pink line Fig. 6), there is no clear east–west distinction in Moho depth. Instead, alternating bands of thick and thin Moho (north to south) are consistent with the estimates of the GOMA seismic reflection line (Korsch et al., 2010a) and BILBY array (Sippl, 2016), indicated by the long N-S transect located just west of the Lake Eyre array stations.

5. Interpretation and discussion

Given a large number of stations in the study, it becomes feasible to use tools like common-conversion point (CCP) stacking to help visualise the Moho topography within the array. For a cross-section, RFs are propagated to 50 km depth using iasp91 velocity model (Kennett and Engdahl, 1991), shown as red crosses in Fig. 7a, and stacked according to rectangular bins (5 km wide). Although the RFs are sediment corrected, the sediment delay is still present, thus we strictly only use the CCP-50 km depth stack to visualise Moho variations rather than to infer depths. For the CCP-50 km stack, stations 80 km on either side of cross-section were included.

5.1. NW-SE variations in Moho and crustal structure (Warumpi to Gawler)

The active seismic GOMA line (abbreviated from Gawler Craton–Officer Basin-Musgrave Province-Amadeus Basin/Warumpi Province) trends almost N-S, starting in the Warumpi Province, extending 643 south, to meet the E-W Eucla-Gawler seismic line (EC-GW, Fig. 1a) in the interior of the Mesoarchean to Mesoproterozoic Gawler Craton. The seismic line traverses the major domains and structures in the region almost perpendicularly; however, most of the traverse is over a concealed basement. As can be seen in Fig. 6, this N-S trending transect illuminates undulating variations in the Moho depth along strike, and includes sharp Moho offsets that bound a shallow Moho (~35 km) centered upon the Musgrave Province. A similar pattern is seen in the Bouguer gravity anomaly for this region (Fig. 8). The east–west trending positive gravity anomaly at latitude 26° S is thought to result from the Petermann orogeny (570–530 Ma; Major and Conor, 1993; Wade et al.,

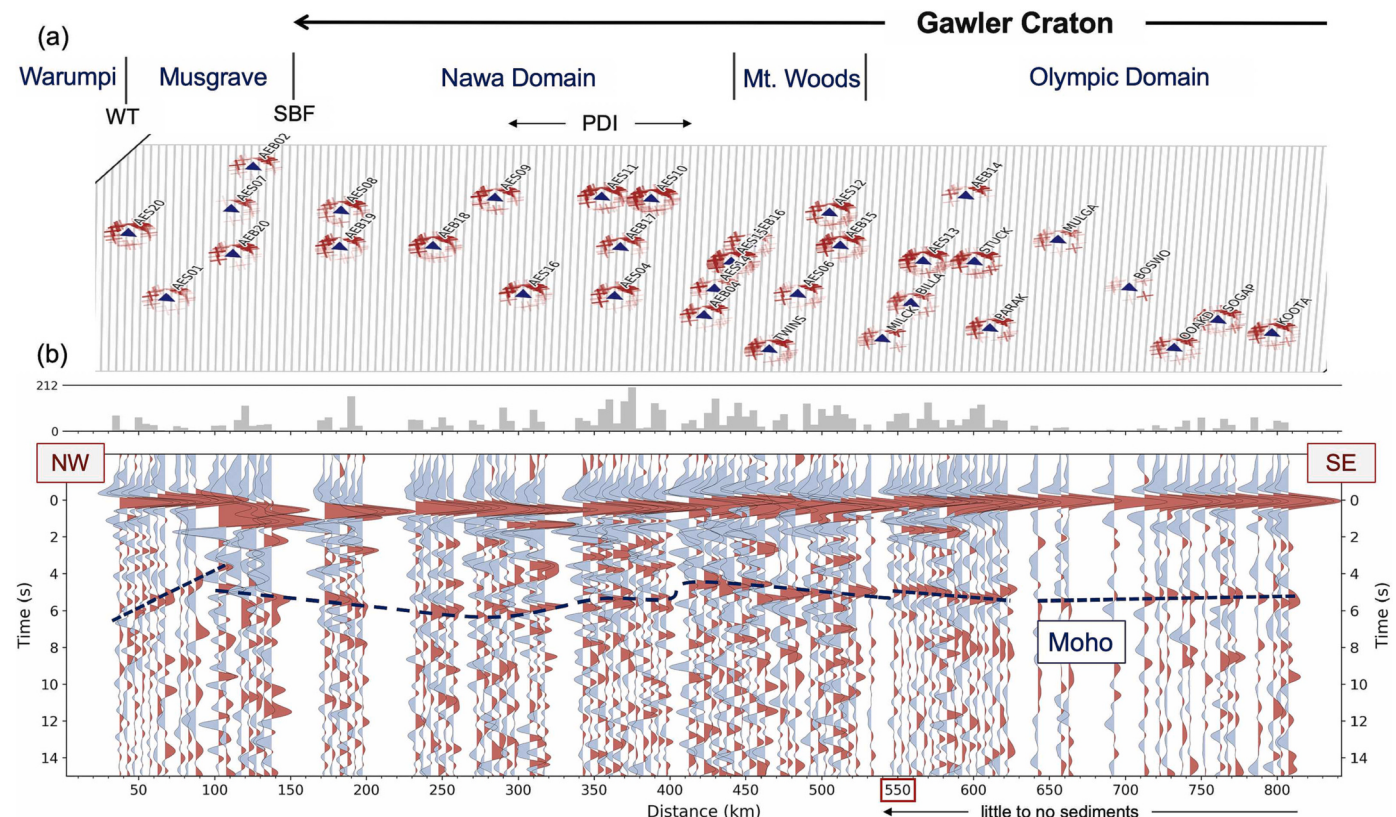


Fig. 7. a) Stations used in the CC' profile (N-W to S-E, refer to Fig. 1a) for common-conversion point stacking at 50 km. Red crosses represent the pierce points at 50 km depth. Grey rectangles indicate bins within which receiver functions are stacked to produce the CCP profile. b) Receiver function stacks for stations along the CC' profile. Top panel displays the number of receiver functions in each bin. The dashed blue line tracks the prominent positive pulse interpreted as the Moho. For the location of the CC' profile and geological provinces, please refer to Figs. 1a and 6, respectively. WT - Woodroffe Thrust Fault, SBF - Sarda Bluff Fault, PDI - Peake and Denison Inlier.

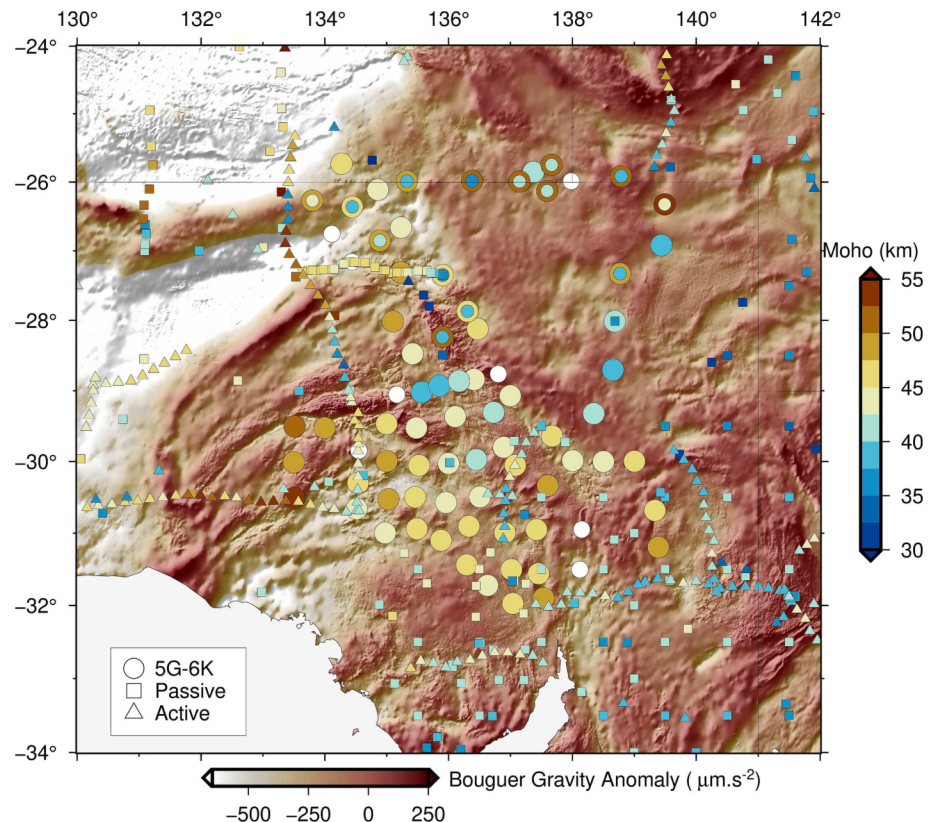


Fig. 8. Same as Fig. 6 but with Bouguer gravity anomalies as the background. The gravity values are obtained from Geoscience Australia's portal (<https://portal.ga.gov.au/>).

2008), which uplifted the crust beneath the Musgrave Province. This uplifted crust is bounded on either side by the Woodroffe Thrust fault in the north and Sarda Bluff Fault in the south, creating the sharp offsets to a deeper Moho on either side (see Korsch et al., 2010a, for a detailed geological interpretation of the GOMA seismic line).

The RFs stack along the CC' profile (Fig. 7) tracks the undulating Moho just east of the GOMA seismic line (Fig. 1a) and extends the transect further down south, until the southern boundary of Lake Torrens within the Gawler Craton (Olympic Domain). Along the ~800 km cross-section, a clear PS_m pulse is identifiable (annotated by a dashed blue line in Fig. 7). The northern end of the profile (0–150 km) samples

the crust under the Warumpi Province and Musgrave Province, which are separated by the south-dipping Woodroffe Thrust fault (WT in Figs. 7 and 9). The Woodroffe fault has been interpreted to cut the entire crust and has been imaged into the lower crust (~48 km), forming the suture between the two geological units (Korsch et al., 2010a). The PS_m pulse under the Warumpi Province is observed to be weakest in the whole CC' profile, suggesting a gradual transition from crust to mantle. This is reinforced by the presence of a diffuse reflective package imaged in the lower crust north of Woodroffe Fault by seismic reflection, with a distinctly different characteristic to the Musgrave Province, to the south (Korsch et al., 2010a). Station AES20 on the Warumpi Province reports a

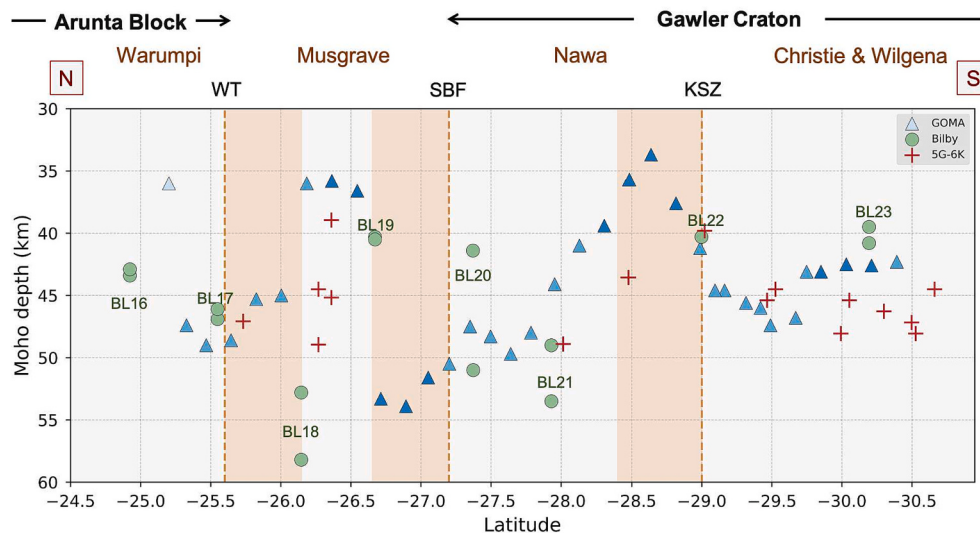


Fig. 9. Comparison of Moho depth estimates between GOMA seismic line (Korsch et al., 2010a), nearby stations of Lake Eyre array (5G) and AusArray-SA (6 K), and coincident BILBY stations (Sippl, 2016). GOMA line estimates (triangles) are coloured such that darker shades reflect locations with higher confidence in the picked Moho. The orange shaded area represents the crustal extent of the faults, while the dashed line marks the surface exposure. WT - Woodroffe Thrust Fault, SBF - Sarda Bluff Fault, KSZ - Karari Shear Zone.

Moho depth of 47 km, which when directly compared to previous studies (Fig. 9), is in good agreement with the H- κ grid search determined Moho (46 km) at station BL17 of the Bilby array (Sippl, 2016). Moho values from the GOMA seismic line (blue triangles Fig. 9) at the same latitude as station AES20 are slightly deeper (~48–49 km) but also similar. It is important to note here that Fig. 7 follows CC' profile while Fig. 9 follows the GOMA seismic line (Fig. 1a), however, the two different cross-sections converge beneath the Warumpi and Musgrave Province.

As previously mentioned the crust of the Musgrave Province is known to be uplifted by 15–20 km (e.g. Aitken et al., 2009), bounded on either side by shallowly dipping crustal scale thrust faults (i.e. the Woodroffe and Sandra Bluff faults). This uplifted crust of the Musgrave Province is clearly visible from active seismic studies (e.g. Fig. S6a) as well as gravity anomalies (Fig. 8). Interpretation of the GOMA seismic reflection line determined a relatively shallow Moho depth of 36 km beneath the centre of the Musgrave Province (Fig. 9). Receiver function Moho estimates at BILBY station BL19 recorded a similarly shallow Moho depth of ~ 40 km (Sippl, 2016). Our results from Lake Eyre stations located within the Musgrave province are more variable but show intriguing patterns. Several of these stations, such as AES01, AEB20, and AEB02 were found to have a double PS_m phase (inner and outer circles Fig. 6), with possible back-azimuthal trends. The station closest to the GOMA line, station AES01, indicated a deeper Moho value of 49 km for northernly back-azimuths (Fig. 4b) that most likely sampled the deeper crust of the Warumpi Province to the north. Meanwhile south-east back-azimuths returned a shallower Moho estimate of 44 km. Other double PS_m stations within the Musgrave Province, AEB20 and AEB02, gave even shallower estimates of 39 and 38 km respectively for the upper of the two Moho picks, which is similar to the previous estimates of the uplifted Musgrave crust (~36–40 km). It is therefore possible that the double PS_m picks in this region are due to the existence of shallowly dipping crustal faults and offsets, with different backazimuths sensitive to either the uplifted Musgrave block, deeper provinces on either side, or a combination of both. The start of the CC' profile in Fig. 7 beneath the Musgrave province also hints at the existence of a Moho structure that is dipping towards the northwest. Such a structure would be consistent with the northwards dipping Sandra Bluff Fault (SBF) which separates the Musgrave and Nawa Provinces (Korsch et al., 2010a). However we note that in Fig. 7 the CCP stack is based on a propagation to 50 km depth and therefore shallower or deeper features which may appear in the CCP profile can not be directly interpreted.

The Nawa Domain is one of the largest domains within the Gawler Craton and the Sandra Bluff Fault marks its northern most extent (Figs. 6 and 7). Across the Nawa Domain from north to south, the GOMA seismic line imaged a shallowing Moho from its deepest values of ~54 km at 27° S to its shallowest value of 34 km at 28.5° S (Fig. 9). The three Lake Eyre stations with results closest to the GOMA line (AES16, AES04, and AEB04) also indicate that the Moho gets shallower from North to South in a similar trend (red crosses Fig. 9). The CC' profile is positioned further east in the Nawa Domain and includes more stations (Fig. 7), but shows a flatter or more gently undulating Moho topography from north to south.

Across the Nawa Domain, however, there are crustal differences from east to west, most notably the presence of a basement outcrop known as the Peake and Denison Inlier (red shaded area in Fig. 6). Previous Moho measurements around this inlier based on temporary seismometer deployments (TL12 and SD06) and one permanent station (OOD) had reported unusually shallow crust of 25–30 km (Kennett et al., 2011). Auto-correlation and RF studies along the Marla Line deployment, a dense east–west transect ~27.5° S, revealed Moho depths between 40–50 km that became shallower further east (Liang and Kennett, 2020). It was suggested that the previous shallow (<30 km) Moho measurements possibly picked up a mid-crustal reflector rather than the base of the crust. We see evidence for such a mid-crustal reflector (~25 km deep), which may have been misinterpreted as the Moho by previous studies. Moho

depths obtained from our seven new stations in the vicinity of the Peake and Denison Inlier and the Marla Line point towards a 45–50 km thick crust (Figs. 6 and 7). This in agreement with the findings of Liang and Kennett (2020), and confirms that the Moho is not unusually thin in this region as initially suggested by the earlier studies (Kennett et al., 2011; Salmon et al., 2013; Qashqai et al., 2019).

Intriguingly, we also find new evidence that the Moho may be ~5 km shallower beneath the Peake and Denison Inlier. This is evident in individual RFs for stations for AES16 and AES04 (Fig. 4d) which display a shallower Moho for eastern backazimuths (towards the inlier) compared to northern backazimuths. Station AEB17 that sits directly atop the inlier was also found to have a double PS_m pick (Fig. 6) indicating complexity in the crustal structure beneath this station that was differs from most of the other surrounding sites. Using rock samples from the drill hole TB02 in the Peake and Denison Inlier, Reid et al. (2017) suggested a similarity to the Aileron Province of the Arunta Region in central Australia. New insights on the Moho beneath the Peake and Denison Inlier are thus important for future tectonic models for Proterozoic Australia as the inlier serves as a potential connection between the North Australian Craton and the Gawler Craton (e.g. Cawood and Korsch, 2008; Howlett et al., 2015).

South of the inlier along the C-C' transect, the Nawa Domain transitions into the smaller Mt Woods Domain obscured by Permian sediments of the Arkaroola Basin, which is manifested as noisier RF signal (410–550 km in Fig. 7). Nonetheless, a strong Moho signature with some undulations can be readily appreciated from the RF. The eight stations in this region are located atop different sedimentary thicknesses, contributing to the noise in the stacked RFs. Notably, four stations (west to east: AEB04, AES14, AES15, and AEB16) deployed in a straight line all show a slightly thinner crust ~ 40 km (light blue circles Fig. 6) compared to stations north and south. A similar pattern of thinning (Moho depths ~ 38 km) was observed from the GOMA seismic line around a latitude of 29° S (Korsch et al., 2010a).

The 550 km point in the C-C' cross-section (highlighted by the red box in Fig. 7b) marks a significant change in both the sedimentary and the crustal structure. At this location the overlying sediments of the Eromanga Basin terminates and the Mt Woods domain transitions to the Olympic which hosts Paleo- to Meso-proterozoic volcanic suites (e.g. Hand et al., 2007). Due to little to no sediments for the remaining stations on the cross-section (550–800 km), the stacked RFs display a much cleaner and impulsive Moho signal with considerably less noise (Fig. 7). The crustal thickness estimates for all the stations within the Olympic Domain are consistently between 43–46 km, suggesting a reasonably flat Moho topography. This is perhaps surprising given that the crust in this region has been substantially modified by the Gawler Range volcanics (c. 1590 Ma), which was the last major event to influence the basement geology of the Gawler Craton (e.g. Hand et al., 2007). The active seismic line in the region - 03GA-OD1/2 (Fig. S6c) however generally matches well (within ±2 km) with our obtained Moho estimates (Drummond et al., 2006).

5.2. Nature of the crust under Lake Eyre Basin and the Simpson Desert

Given the lack of outcrops in the northeastern part of South Australia, there is limited information about the age and the nature of the underlying basement in the region. As such it is unclear whether this region falls east or west of the Tasman Line, whether the crustal basement belongs to either Precambrian or Phanerozoic Australia. Previously the best constraint on the crustal structure beneath his region came from a recent N-S trending seismic line 14-CF2 terminating at Birdsville in the southwest corner of Queensland (see Fig. 1a for location). At the southernmost point in the reflection profile, a clear sharp Moho reflector is seen around 36 km (Fig. S6d). For the closest stations, AEB10 and AEB07, we reported two Moho depths, with the shallower depths being 39.40 km and 41.90 km, respectively (Fig. 6). Even though our estimates are slightly higher than those from the seismic line, it does

suggest that our picked PS_m pulses are likely due to the Moho conversion.

For many stations across the Lake Eyre region (yellow shaded area Fig. 6), and in particular across the Simpson Desert, these stations display double Moho picks. They are also located on thick sediments (> 800 m) and therefore were not able to be corrected using the sediment reverberation filter, thus these stations were substantially noisier than others. Interestingly, the upper estimates from stations in this region are all consistent (39–42 km) suggesting coherent structure; on the other hand, the deeper Moho estimates fall in a significantly wider range (47–53 km). The consistency and correlation of the shallower Moho estimates with the 14-CF2 active seismic line suggest that the Moho depth is most likely in the range 39–42 km. We therefore use these shallower estimates for further analysis of the crustal signature within this region.

A recent tomography study of the Australian continent using ambient seismic noise data revealed the shear-wave velocities in the crust and lithosphere across Australia and including the Lake Eyre region (Chen et al., 2021). Using shear-wave velocity contours between 4.3 km/s and 4.6 km/s as a proxy for the crust to mantle transition, they extracted a Moho surface and compared it to two other continental Moho models, (i) AusMoho (Kennett et al., 2011), and (ii) a P-wave coda auto-correlation derived Moho (Qashqai et al., 2019). Notably, they reported a thicker Moho (by about 10 km) in the Lake Eyre region (northeastern edge of the Gawler Craton) compared to the two former studies. Although Chen et al. (2021)'s Moho estimates are indirectly accessed from the velocity profiles, they fit surprisingly well with our RF measurements acquired from a completely independent dataset.

We can further compare our Moho estimates for different geological provinces based on the geographical location of the seismic stations. Across our network the stations are primarily located on either the Gawler Craton, the Musgrave Province, or the Lake Eyre region under which the nature of the basement is unknown. The Moho depth distributions (for our RF-based measurements and the seismic reflection lines) in each province are shown as density violins in Fig. 10. As mentioned above, for the stations in the Lake Eyre region, only the shallower (i.e. consistent) Moho estimates are used, thus resulting in a more compact

distribution with a median Moho depth of ~ 41 km. Contrastingly, for the Gawler Craton, both the active and passive measurements conform to a more classical bell-shaped density plot, with a median Moho value of ~ 45 km. This further confirms the visual trend of generally flat Moho topography under the Gawler Craton, as seen from the AusArray-SA stations in Fig. 6, except for the slightly thinner crust under the Peake and Denison Inlier. As expected, for the Musgrave Province (Fig. 10), Moho depths vary considerably owing to the uplifted crust (Wade et al., 2008) and the bounding in-dipping faults on both sides (Fig. 9). This resulted in a more elongated distribution.

Although the stations used in this study do not extend as far as the Curnamona Craton, two seismic lines 09-C1 and 03-CU1 (see Fig. 1a for location), densely sample the craton providing useful Moho constraints for comparison. Interestingly, the median crustal thickness obtained from the seismic reflection profile is ~ 41 km (Korsch et al., 2010b), which is similar to what is observed under the Lake Eyre region (Fig. 10). Although both methods use different time-to-depth conversions and have their associated uncertainties, the correspondence between the Moho distributions hints towards a possible shared Proterozoic tectonic history. Further east of the Lake Eyre region, in Phanerozoic Australia, the crustal thickness is even thinner (~ 35 km) in the Thomson and Lachlan Orogens (Glen, 2005; Kennett et al., 2011; Spampinato et al., 2015). This would suggest that the basement beneath the Lake Eyre region is more similar to the Proterozoic crust beneath Curnamona, at least in terms of thickness, than the Phanerozoic crust further east. If such a Proterozoic origin of the Lake Eyre region basement exists then this would place a possible boundary with Phanerozoic Australia (e.g. the Tasman Line) somewhere east of the 140° longitude.

The western extent of the Thomson Orogen is however essentially undefined due to the lack of surface rock outcrops across the region (dotted lines in Fig. 6). Beneath the Lake Eyre region lies a long history of sedimentation, the oldest of which is the Cambrian-Ordovician Warburton Basin (see Fig. 1 of Agrawal et al., 2022). Some studies have included the Warburton Basin into the Thomson Orogen based on the thin-extended crust of the central and north Thompson Orogen (associated with back-arc extension in response to trench retreat; Glen, 2005; Glen, 2013; Spampinato et al., 2015; Rosenbaum, 2018) that



Fig. 10. Moho depth distribution showcased as violin density plot for the geological provinces in the study region. Red violins are Moho estimates from seismic reflection lines, while yellow are receiver function-based measurements from this study. The white circle denotes the median, while the black bar represents the upper and lower quartiles. The number of measurements in each violin is printed at the top.

matched with the perceived thin crust beneath Lake Eyre Region (~ 30 km). However, we suggest that the western extent of Thompson should be reconsidered and perhaps not include Warburton Basin. Recent work by Abdullah et al. (2019) suggested a curved northward continuation of the Delamerian Belt in the eastern Warburton Basin (east of the Birdsville Track, annotated in Fig. 1a), which would put the boundary of the Delamerian Orogen east of the Lake Eyre Region. The thicker crust found beneath the Lake Eyre Region thus has significant implications for the tectonic relationship of the Thomson and Delamerian Orogens with Proterozoic Australia, and for the Paleozoic subduction processes (such as the trench retreat or advance; Glen, 2013; Rosenbaum, 2018; Abdullah et al., 2019) along the eastern Gondwana margin.

6. Conclusion

In this study, we utilised two recently completed seismic arrays in South Australia, Lake Eyre Basin array and AusArray-SA, which included seismic stations on regions of exposed outcrop to heavily sedimented areas (up to 3000 m). Using the resonance removal filter technique developed by Yu et al. (2015), we were able to suppress the reverberatory energy from the sedimentary layer in the receiver functions and consequently image the Moho structure across the region. We found that the method works best for stations where the Phanerozoic sedimentary cover thickness is less than 800 m, or in other words, where a dominant resonance frequency associated with the sediments can be found. The protocols established in this study to assess and correct sediment-impacted receiver functions may aid future passive seismic experiments that expand across regions of varying degree of sedimentation. Upcoming large scale deployments, such as the WA-array, that aim to characterise the crustal structure across the entire state of Western Australia in the coming decade, will need to take such factors into account.

Our sediment-corrected receiver functions illuminated the Moho variations across the study region, both within the Gawler Craton and along its eastern margin. Comparison with active seismic reflection profiles in and around the area shows similarity with our Moho estimates. Most importantly, we provide new constraints on the crust of a hitherto under-explored part of South Australia, i.e., the region lying beneath Lake Eyre Basin and the Simpson Desert. Previous studies had reported an abnormally thin crust of around 30 km, albeit based on sparse observations. Based on increased station coverage, we now estimate a crustal thickness of up to 43 km, which is similar to the median crustal thickness in nearby Proterozoic regions such as the Curnamona Province. Such estimates are consistent with a Proterozoic basement underlying the Lake Eyre region and Warburton Basin, and would suggest that the area should perhaps be included with western Precambrian Australia, rather than the younger eastern Tasmanides.

Data and resources

The earthquakes used in this study were collected from Incorporated Research Institutions for Seismology (IRIS) Data Services (<http://ds.iris.edu/ds/>). The seismic waveform data from two seismic networks was used: 5G (https://doi.org/10.7914/SN/5G_2018); 6 K (https://doi.org/10.7914/SN/6K_2020). The Python package ‘rf’ version 1.0.0 (Eulenberg, 2020) was used to compute the RFs with some help from HiPerSies package (<https://github.com/GeoscienceAustralia/hiperseis>; Hassan et al., 2020). All the seismic data were handled using the Python package Obspy (<https://docs.obspy.org/>; Krischer et al., 2015). Plots were made using the Generic Mapping Tools, Version 6.1.1 (<https://www.generic-mapping-tools.org/>; Wessel et al., 2019) and Matplotlib version 3.4.2 (<https://matplotlib.org/>).

CRediT authorship contribution statement

Shubham Agrawal: Conceptualization, Investigation, Writing-

original-draft. **Caroline M. Eakin:** Conceptualization, Investigation, Writing-review-editing. **John P. O'Donnell:** Investigation, Writing-review-editing, Resources.

Declaration of Competing Interest

The authors declare that they have no known competing financial interests or personal relationships that could have appeared to influence the work reported in this paper.

Data availability

The seismic data would be made available automatically on auspass.edu.au/ after the legacy period ends.

Acknowledgments

We acknowledge the traditional custodians - past, present, and emerging - of South Australia on whose land the seismic stations were deployed. We thank the reviewers for their constructive comments and suggestions. SA and CE are supported by Australian Research Council grant DE190100062. The Lake Eyre Basin seismic array and many other previous temporary deployments were made possible via funding from AuScope (<https://auscope.org.au>), instrumentation from the Australian National Seismic Imaging Resource (ANSIR), and contributions from staff, especially Robert Pickle and Michelle Salmon, at the Research School of Earth Sciences, Australian National University. The AusArray SA deployment is supported by the Geological Survey of South Australia, with instrumentation from ANSIR and Geoscience Australia. The Geological Survey of South Australia thanks Ann Goleby, Isaac Axford, Kate Selway, Bruce Goleby, John Stephenson, Alexei Gorbatov, and Colin Telfer for their contribution to AusArray SA. We are incredibly grateful to landholders, traditional owners, and the Department of Defence for granting land access for the seismic arrays. JPOD publishes with the permission of the Director of the Geological Survey of Western Australia.

Appendix A. Supplementary data

Supplementary data associated with this article can be found, in the online version, at <https://doi.org/10.1016/j.tecto.2023.229938>.

References

- Abdullah, R., Nugroho, R., Rosenbaum, G., Doublier, M.P., Shaanan, U., Zwingmann, H., 2019. Evidence for deformation in the cambrian-ordovician warburton basin and implications for the evolution of the tasmanides (eastern australia). *Tectonics* 38, 1532–1555.
- Abramovitz, T., Berthelsen, A., Thybo, H., 1997. Proterozoic sutures and terranes in the southeastern baltic shield interpreted from babel deep seismic data. *Tectonophysics* 270, 259–277.
- Agrawal, S., Eakin, C.M., O'Donnell, J., 2022. Characterizing the cover across south australia: A simple passive-seismic method for estimating sedimentary thickness. *Geophys. J. Int.* 231, 1850–1864.
- Aitken, A., Salmon, M., Kennett, B., 2013. Australia's moho: a test of the usefulness of gravity modelling for the determination of moho depth. *Tectonophysics* 609, 468–479.
- Aitken, A.R., Betts, P.G., Weinberg, R.F., Gray, D., 2009. Constrained potential field modeling of the crustal architecture of the musgrave province in central australia: Evidence for lithospheric strengthening due to crust-mantle boundary uplift. *J. Geophys. Res.: Solid Earth* 114.
- Ammon, C.J., 1991. The isolation of receiver effects from teleseismic p waveforms. *Bull. Seismol. Soc. Am.* 81, 2504–2510.
- Betts, P.G., Giles, D., Lister, G., Frick, L., 2002. Evolution of the australian lithosphere. *Aust. J. Earth Sci.* 49, 661–695.
- Bodin, T., Sambridge, M., Tkalcic, H., Arroucau, P., Gallagher, K., Rawlinson, N., 2012. Transdimensional inversion of receiver functions and surface wave dispersion. *J. Geophys. Res.: Solid Earth* 117.
- Cawood, P.A., Korsch, R., 2008. Assembling australia: Proterozoic building of a continent. *Precambrian Res.* 166, 1–35.
- Chen, Y., Saygin, E., Kennett, B., Tork Qashqai, M., Hauser, J., Lumley, D., Sandiford, M., 2021. Next-generation velocity model of the australian crust from synchronous and

- asynchronous ambient noise imaging. v1. URL:<https://doi.org/10.25919/m2a2-qb97>. doi: 10.25919/m2a2-qb97.
- Clitheroe, G., Gudmundsson, O., Kennett, B., 2000. The crustal thickness of australia. *J. Geophys. Res.: Solid Earth* 105, 13697–13713.
- Clitheroe, G., Gudmundsson, O., Kennett, B., 2000. Sedimentary and upper crustal structure of australia from receiver functions. *Aust. J. Earth Sci.* 47, 209–216.
- Collins, C., Drummond, B., Nicoll, M., 2003. Crustal thickness patterns in the australian continent. *Spec. Pap. Geol. Soc. Am.* 121–128.
- Cunningham, E., Lekic, V., 2019. Constraining crustal structure in the presence of sediment: a multiple converted wave approach. *Geophys. J. Int.* 219, 313–327.
- Diaconescu, C.C., Knapp, J.H., Brown, L.D., Steer, D.N., Stiller, M., 1998. Precambrian moho offset and tectonic stability of the east european platform from the urseis deep seismic profile. *Geology* 26, 211–214.
- Direen, N., Crawford, A., 2003. The tasman line: where is it, what is it, and is it australia's rodinian breakup boundary? *Aust. J. Earth Sci.* 50, 491–502.
- Drummond, B., Lyons, P., Goleby, B., Jones, L., 2006. Constraining models of the tectonic setting of the giant olympic dam iron oxide–copper–gold deposit, south australia, using deep seismic reflection data. *Tectonophysics* 420, 91–103.
- Eakin, C., 2019. Seismicity, minerals, and craton margins: The lake eye basin seismic deployment. *ASEG Extend. Abstr.* 2019, 1–2.
- Eaton, D.W., 2006. Multi-genetic origin of the continental moho: Insights from lithoprobe. *Terra Nova* 18, 34–43.
- Eulenfeld, T., 2020. rf: Receiver function calculation in seismology. *J. Open Source Softw.* 5, 1808.
- Fraser, G., McAvaney, S., Neumann, N., Szpunar, M., Reid, A., 2010. Discovery of early mesoarchean crust in the eastern gawler craton, south australia. *Precambr. Res.* 179, 1–21.
- Gatehouse, C.G., 1986. The geology of the warburton basin in south australia. *Aust. J. Earth Sci.* 33, 161–180.
- Glen, R., 2005. The tasmanides of eastern australia. *Spec. Publ. Geol. Soc. Lond.* 246, 23.
- Glen, R., 2013. Refining accretionary orogen models for the tasmanides of eastern australia. *Aust. J. Earth Sci.* 60, 315–370.
- Gorbatov, A., Saygin, E., Kennett, B., 2013. Crustal properties from seismic station autocorrelograms. *Geophys. J. Int.* 192, 861–870.
- Habeck-Fardy, A., Nanson, G.C., 2014. Environmental character and history of the lake eye basin, one seventh of the australian continent. *Earth Sci. Rev.* 132, 39–66.
- Hand, M., Reid, A., Jagodzinski, L., 2007. Tectonic framework and evolution of the gawler craton, southern australia. *Econ. Geol.* 102, 1377–1395.
- Hassan, R., Hejraní, B., Zhang, F., Gorbatov, A., Medlin, A., 2020. High-performance seismological tools (HiPerSeis). *Geoscience Australia*.
- Howlett, D., Raimondo, T., Hand, M., 2015. Evidence for 1808–1770 ma bimodal magmatism, sedimentation, high-temperature deformation and metamorphism in the aileron province, central australia. *Aust. J. Earth Sci.* 62, 831–852.
- Julia, J., Ammon, C., Herrmann, R., Correig, A.M., 2000. Joint inversion of receiver function and surface wave dispersion observations. *Geophys. J. Int.* 143, 99–112.
- Kennett, B., Chopping, R., Blewett, R., 2018. The Australian continent: A geophysical synthesis. ANU Press.
- Kennett, B., Engdahl, E., 1991. Traveltimes for global earthquake location and phase identification. *Geophys. J. Int.* 105, 429–465.
- Kennett, B., Salmon, M., Saygin, E., Group, A.W., 2011. Ausmoho: the variation of moho depth in australia. *Geophys. J. Int.* 187, 946–958.
- Kennett, B., Saygin, E., 2015. The nature of the moho in australia from reflection profiling: a review. *GeoResJ* 5, 74–91.
- Kennett, B., Saygin, E., Fomin, T., Blewett, R., 2016. Deep Crustal Seismic Reflection Profiling: Australia 1978–2015. ANU Press and Geoscience Australia.
- Korsch, R., Blewett, R., Giles, D., Reid, A., Neumann, N., Fraser, G., Holzshuh, J., Costelloe, R., Roy, I., Kennett, B., et al., 2010a. Geological interpretation of the deep seismic reflection and magnetotelluric line 08ga-om1: Gawler craton-officer basin-musgrave province-amadeus basin (goma), south australia and northern territory. In: GOMA (Gawler Craton-Officer Basin-Musgrave Province-Amadeus Basin) Seismic and MT Workshop, pp. 63–86.
- Korsch, R., Dublier, M., 2016. Major crustal boundaries of australia, and their significance in mineral systems targeting. *Ore Geol. Rev.* 76, 211–228.
- Korsch, R., Preiss, W., Blewett, R., Fabris, A., Neumann, N., Fricke, C., Fraser, G., Holzschuh, J., Milligan, P., Jones, L., 2010b. Geological interpretation of deep seismic reflection and magnetotelluric line 08ga-c1: Curnamona province, south australia. In: South Australian Seismic and MT Workshop, Extended Abstracts. Geoscience Australia Record, pp. 42–53.
- Krischer, L., Megies, T., Barsch, R., Beyreuther, M., Lecocq, T., Caudron, C., Wassermann, J., 2015. Obspy: A bridge for seismology into the scientific python ecosystem. *Comput. Struct. Discov.* 8, 014003.
- Langston, C.A., 1979. Structure under mount rainier, washington, inferred from teleseismic body waves. *J. Geophys. Res.: Solid Earth* 84, 4749–4762.
- Langston, C.A., 2011. Wave-field continuation and decomposition for passive seismic imaging under deep unconsolidated sediments. *Bull. Seismol. Soc. Am.* 101, 2176–2190.
- Laske, G., Masters, G., Ma, Z., Pasyanos, M., 2013. Update on crust1. 0—a 1-degree global model of earth's crust. In: Geophysical research abstracts. EGU General Assembly Vienna, Austria, p. 2658.
- Leahy, G.M., Saltzer, R.L., Schmedes, J., 2012. Imaging the shallow crust with teleseismic receiver functions. *Geophys. J. Int.* 191, 627–636.
- Liang, S., Kennett, B., 2020. Passive seismic imaging of a craton edge—central australia. *Tectonophysics* 797, 228662.
- Ligorria, J.P., Ammon, C.J., 1999. Iterative deconvolution and receiver-function estimation. *Bull. Seismol. Soc. Am.* 89, 1395–1400.
- Lloyd, J.C., Blades, M.L., Counts, J.W., Collins, A.S., Amos, K.J., Wade, B.P., Hall, J.W., Hore, S., Ball, A.L., Shahin, S., et al., 2020. Neoproterozoic geochronology and provenance of the adelaide superbasin. *Precambr. Res.* 350, 105849.
- Major, R., Conor, C., 1993. Musgrave block. *Geol. South Aust.* 1, 156–167.
- Meixner, T.J., Gunn, P.J., Boucher, R.K., Yeates, T.N., Richardson, L.M., Frears, R.A., 2000. The nature of the basement to the cooper basin region, south australia. *Explor. Geophys.* 31, 24–32.
- Myers, J.S., 1990. Precambrian tectonic evolution of part of gondwana, southwestern australia. *Geology* 18, 537–540.
- O'Donnell, J., Thiel, S., Robertson, K., Gorbatov, A., Eakin, C., 2020a. Using seismic tomography to inform mineral exploration in south australia: The ausarray sa broadband seismic array. *MESA J.* 93, 24–31.
- O'Donnell, J., Thiel, S., Robertson, K., Gorbatov, A., Goleby, B., 2020b. Ausarray sa. URL: https://www.fdsn.org/networks/detail/6K_2020/. doi: 10.7914/SN/6K_2020.
- Parker Jr., E.H., Hawman, R.B., Fischer, K.M., Wagner, L.S., 2016. Estimating crustal thickness using sspmp in regions covered by low-velocity sediments: Imaging the moho beneath the southeastern suture of the appalachian margin experiment (sesame) array, se atlantic coastal plain. *Geophys. Res. Lett.* 43, 9627–9635.
- Piana Agostinetti, N., Martini, F., Mongan, J., 2018. Sedimentary basin investigation using receiver function: an east african rift case study. *Geophys. J. Int.* 215, 2105–2113.
- Preiss, W., 2000. The adelaide geosyncline of south australia and its significance in neoproterozoic continental reconstruction. *Precambr. Res.* 100, 21–63.
- Qashqai, M., Saygin, E., Kennett, B., 2019. Crustal imaging with bayesian inversion of teleseismic p wave coda autocorrelation. *J. Geophys. Res.: Solid Earth* 124, 5888–5906.
- Raymond, O., Totterdell, J., Woods, M., Stewart, A.J., 2018. Australian geological provinces 2018.01 edition. Geoscience Australia, Canberra.
- Reid, A., 2019. The olympic cu-au province, gawler craton: a review of the lithospheric architecture, geodynamic setting, alteration systems, cover successions and prospectivity. *Minerals* 9, 371.
- Reid, A.J., Jagodzinski, E.A., Wade, C.E., Payne, J.L., Jourdan, F., 2017. Recognition of c. 1780 ma magmatism and metamorphism in the buried northeastern gawler craton: Correlations with events of the aileron province. *Precambr. Res.* 302, 198–220.
- Rosenbaum, G., 2018. The tasmanides: Phanerozoic tectonic evolution of eastern australia. *Annu. Rev. Earth Planet. Sci.* 46, 291–325.
- Salmon, M., Kennett, B., Saygin, E., 2013. Australian seismological reference model (ausrem): crustal component. *Geophys. J. Int.* 192, 190–206.
- Salmon, M., Kennett, B., Stern, T., Aitken, A., 2013. The moho in australia and new zealand. *Tectonophysics* 609, 288–298.
- Shaw, R., Wellman, P., Gunn, P., Whitaker, A., Tarlowski, C., Morse, M., 1995. Australian crustal elements map. AGSO Res. Newslett. 23, 1–3.
- Sippl, C., 2016. Moho geometry along a north–south passive seismic transect through central australia. *Tectonophysics* 676, 56–69.
- Skirrow, R.G., Bastrakov, E.N., Barovich, K., Fraser, G.L., Creaser, R.A., Fanning, C.M., Raymond, O.L., Davidson, G.J., 2007. Timing of iron oxide cu-au-(u) hydrothermal activity and nd isotope constraints on metal sources in the gawler craton, south australia. *Econ. Geol.* 102, 1441–1470.
- Spampinato, G.P., Betts, P.G., Ailleres, L., Armit, R.J., 2015. Early tectonic evolution of the thomson orogen in queensland inferred from constrained magnetic and gravity data. *Tectonophysics* 651, 99–120.
- Srinivas, D., Srinagesh, D., Chadha, R., Ravi Kumar, M., 2013. Sedimentary thickness variations in the indo-gangetic foredeep from inversion of receiver functions. *Bull. Seismol. Soc. Am.* 103, 2257–2265.
- Stern, T., McBride, J., 1998. Seismic exploration of continental strike-slip zones. *Tectonophysics* 286, 63–78.
- Tao, K., Liu, T., Ning, J., Niu, F., 2014. Estimating sedimentary and crustal structure using wavefield continuation: theory, techniques and applications. *Geophys. J. Int.* 197, 443–457.
- Vinnik, L., 1977. Detection of waves converted from p to sv in the mantle. *Phys. Earth Planet. Inter.* 15, 39–45.
- Wade, B., Kelsey, D., Hand, M., Barovich, K., 2008. The musgrave province: stitching north, west and south australia. *Precambr. Res.* 166, 370–386.
- Wang, C., Tauzin, B., Pham, T.S., Tkalcic, H., 2020. On the efficiency of p-wave coda autocorrelation in recovering crustal structure: Examples from dense arrays in the eastern united states. *J. Geophys. Res.: Solid Earth* 125, e2020JB020270.
- Wessel, P., Luis, J., Uieda, L., Scharroo, R., Wobbe, F., Smith, W., Tian, D., 2019. The generic mapping tools version 6. *Geochem. Geophys. Geosyst.* 20, 5556–5564.
- Wise, T., Thiel, S., 2020. Proterozoic tectonothermal processes imaged with magnetotellurics and seismic reflection in southern australia. *Geosci. Front.* 11, 885–893.
- Wittlinger, G., Vergne, J., Tapponnier, P., Farra, V., Poupinet, G., Jiang, M., Su, H., Herquel, G., Paul, A., 2004. Teleseismic imaging of subducting lithosphere and moho offsets beneath western tibet. *Earth Planet. Sci. Lett.* 221, 117–130.
- Yeck, W.L., Sheehan, A.F., Schulte-Pelkum, V., 2013. Sequential h-k stacking to obtain accurate crustal thicknesses beneath sedimentary basins. *Bull. Seismol. Soc. Am.* 103, 2142–2150.
- Yu, Y., Song, J., Liu, K.H., Gao, S.S., 2015. Determining crustal structure beneath seismic stations overlying a low-velocity sedimentary layer using receiver functions. *J. Geophys. Res.: Solid Earth* 120, 3208–3218.
- Zelt, B., Ellis, R., 1999. Receiver-function studies in the trans-hudson orogen, saskatchewan. *Can. J. Earth Sci.* 36, 585–603.
- Zhang, P., Yao, H., Chen, L., Fang, L., Wu, Y., Feng, J., 2019. Moho depth variations from receiver function imaging in the northeastern north china craton and its tectonic implications. *J. Geophys. Res.: Solid Earth* 124, 1852–1870.

- Zhang, Z., Olugboji, T., 2021. The signature and elimination of sediment reverberations on submarine receiver functions. *J. Geophys. Res.: Solid Earth* 126, e2020JB021567.
- Zhu, L., 2000. Crustal structure across the san andreas fault, southern california from teleseismic converted waves. *Earth Planet. Sci. Lett.* 179, 183–190.
- Zhu, L., Kanamori, H., 2000. Moho depth variation in southern california from teleseismic receiver functions. *J. Geophys. Res.: Solid Earth* 105, 2969–2980.